

1 **Testing ground based observations of wave activity in the (lower and upper) atmosphere**  
2 **as possible (complementary) indicators of streamer events**

3 **Michal Kozubek<sup>1</sup>, Lisa Kuchelbacher<sup>2</sup>, Jaroslav Chum<sup>1</sup>, Tereza Sindelarova<sup>1</sup>, Franziska**  
4 **Trinkl<sup>2, a</sup>, Katerina Podolska<sup>1</sup>**

5 <sup>1</sup>Institute of Atmospheric Physics CAS, Bocni II 1401, Prague, 14100, Czech Republic

6 <sup>2</sup> Earth Observation Center, Deutsches Zentrum für Luft- und Raumfahrt, 82234 Weßling,  
7 Germany

8 <sup>a</sup> now at Karlsruhe Institute of Technology (KIT), Institute of Meteorology and Climate  
9 Research, Karlsruhe, Germany

10 **Correspondence: Michal Kozubek, [kom@ufa.cas.cz](mailto:kom@ufa.cas.cz)**

11 **Keywords:** gravity waves, streamer events, infrasound, Doppler measurements

12

13 **Abstract:** For a better understanding of atmospheric dynamics, it is very important to know  
14 the general conditions (dynamics and chemistry) of the atmosphere. Planetary waves (PWs)  
15 are global scale waves, which are well-known as main drivers of the large-scale weather  
16 patterns in mid-latitudes on time scales from several days up to weeks in the troposphere.  
17 When PWs break, they often cut pressure cells off the jet stream. A specific example are so-  
18 called streamer events, which occur predominantly in the lower stratosphere at mid- and high-  
19 latitudes. For streamer events we check, whether there are any changes of gravity wave (GW)  
20 or infrasound characteristics related to these events in ionospheric and surface measurements  
21 (continuous Doppler soundings, two arrays of microbarometers) in the Czech Republic.

22 Phenomena in infrasound arrival parameters undoubtedly related with streamer events were  
23 not identified in observations of two stations located in Central Europe. Simulations of  
24 infrasound propagation show influences of the streamer events on the waveguide formed near  
25 the tropopause. Microbarom propagation is influenced by the tropopause waveguide in a  
26 limited azimuth sector and at limited distances. Due to the typical occurrence of the streamer  
27 events over the North Atlantic, infrasound stations in Western Europe can be of particular  
28 interest for future studies of streamer event signatures in infrasound arrivals. Arrivals to  
29 Central Europe are through the waveguide formed between the ground and the upper  
30 stratosphere. The upper stratosphere waveguide is not influenced by the streamer events.

31 Supplementary ground-based measurements of GW using the WBCI array in the troposphere  
32 showed that GW propagation azimuths were more random during streamer and streamer-like  
33 events compared to those observed during calm conditions. GW propagation characteristics  
34 observed in the ionosphere by continuous Doppler soundings during streamer events did not  
35 differ from those expected for the given time period.

36

## 37 **1) Introduction**

38 For a better comprehension of climate change it is fundamentally important, how well we  
39 understand the climate system in general, and the dynamics of the atmosphere in particular.  
40 The dynamical processes in the atmosphere relevant in this context in the atmosphere take  
41 place over a comparatively wide range of scales in space and time. They include in particular  
42 both, planetary and gravity waves. Planetary waves are one of the main drivers of the  
43 extratropical circulation. When they break, they lead to an irreversible exchange of air masses  
44 between the equatorial and polar region due to an amplification of their amplitudes (e.g.  
45 McIntyre & Palmer, 1983; Polvani & Plumb, 1992). In the lower stratosphere ozone can be  
46 used as a tracer for these large-scale motions, as it has a comparatively long life-time. When  
47 planetary waves break tropical air masses of low ozone concentration are mixed poleward into  
48 the surrounding atmosphere of the mid and higher latitudes (e.g. Leovy et al., 1985).

49 The term "streamer" lacks a precise definition, as noted by Krüger et al. (2005). They  
50 discuss various aspects of streamers, including their impact on mixing and the divergent  
51 definitions associated with them. Offermann et al. (1999) describe streamers as large-scale  
52 tongue-like structures formed by the meridional deflection of air masses. Streamers are  
53 characterized by irreversible mixing of air masses between equatorial and polar regions which  
54 is why they might be linked to planetary wave breaking (Waugh, 1993). Eyring et al. (2003)  
55 give a climatology of the seasonal and geographical distribution of streamer events. They  
56 show, that streamers often occur over the Northern Atlantic and can be identified by either  
57 high NO<sub>2</sub> or low ozone concentration, which is why we select streamers by total ozone  
58 column measurements. Eyring et al. (2003) show that streamer events occur most often during  
59 winter and least during July and August in the Northern Hemisphere. During a streamer event  
60 the wind field changes rather strongly over a comparatively small distance. Since a streamer  
61 event shows a strong wind shear at its flanks, it is expected that it excites GW (e.g. Kramer et  
62 al., 2015 and 2016 or Peters et al., 2003).

63 It is well-known that enhanced wind gradients or anticyclones can lead to the  
64 excitation of gravity waves (GW) in the atmosphere (e.g. Pramitha et al., 2015; Kai et al.,  
65 2010; Kramer et al., 2015, 2016 and Gerlach et al., 2003). GW have typical vertical  
66 wavelengths from a few 100 m to several kilometres (Wüst & Bittner, 2006), and horizontal  
67 wavelengths over tens of km (Wüst et al., 2018), and longer (Rauthe et al., 2006); their  
68 fluctuations in the upper troposphere / lower stratosphere typically show amplitudes of 5–10  
69 m/s at maximum (e.g., Kramer et al., 2015). Those waves transport energy and momentum  
70 horizontally and vertically through the atmosphere and deposit them especially in the  
71 stratosphere and mesosphere but also above and below this height region. The propagation of  
72 GWs is strongly dependent on the wind conditions in the stratosphere since the wind speed of  
73 the middle atmosphere (10–100 km) reaches its maximum there. That is why monitoring  
74 waves in upper parts of the atmosphere, e.g. based on Doppler observations in the ionosphere,  
75 can provide additional information about stratospheric conditions (for details see Fritts and  
76 Alexander, 2003).

77 Using pressure recordings at a microbarograph array, GWs and infrasound at the ground can  
78 be observed. Ground based observations of GWs at a large aperture microbarograph array are  
79 utilized in the present study as an independent data source for the analysis of GW activity  
80 during streamer events. Infrasound propagation is influenced by wind and temperature fields  
81 in the atmosphere. Three regions play an important role in long-distance infrasound  
82 propagation: (1) the lower thermosphere; (2) the stratosphere; (3) the jet stream near the  
83 tropopause and inversion layers in the troposphere (Evers and Haak, 2010). Infrasound  
84 observed at the ground and emitted by distant sources mostly propagates in the stratospheric  
85 waveguide (Ceranna et al., 2019). The thermospheric waveguide is not as efficient as the  
86 stratospheric waveguide in the long-range infrasound propagation. Besides signal loss due to  
87 geometrical spreading, infrasound absorption is important in the upper atmosphere (Bittner et  
88 al., 2010). Infrasound absorption is proportional to the frequency; higher frequencies,  
89 particularly those above 1 Hz undergo stronger absorption in the thermosphere (Sutherland  
90 and Bass, 2004). Signal attenuation is low at frequencies of the order of  $10^{-3} - 10^{-2}$  Hz (Blanc,  
91 1985; Georges, 1968).

92 A number of case studies have proved that stratospheric dynamics can be deduced from  
93 microbarograph measurements at the ground (Assink et al., 2014; Blixt et al., 2019; Evers and  
94 Siegmund, 2009; Evers et al., 2012; Garcès et al., 2004; Le Pichon and Blanc, 2005; Le  
95 Pichon et al., 2006 and 2009; Smets and Evers, 2014). Streamer events are significant

96 transient disturbances to circulation patterns in the tropopause/lower stratosphere region;  
97 modifications of the stratospheric waveguide can therefore be expected. A feasibility study on  
98 utilisation of ground infrasound measurements in research of streamer events is performed  
99 here. Its aim is to identify phenomena in infrasound detections related to the streamers; we  
100 focus on deviations of the azimuth of signal arrivals, trace velocity, signal amplitude, and  
101 frequency. Dedicated studies demonstrated that from the observed signal trace velocity,  
102 information about the signal refraction height can be derived (Lonzaga, 2015). If the source of  
103 received signals is well defined in time and space, mean atmospheric cross-winds along the  
104 signal propagation path can be estimated from back-azimuth deviations and time of signal  
105 propagation (Blixt et al., 2019). Fluctuations of signal frequency and amplitude are, besides  
106 variability of the signal source influenced by atmospheric filtering (Sutherland and Bass,  
107 2004).

108 Our study will focus on the possible utilization Doppler sounding and microbarographs for  
109 description and analysis of GW behaviour and propagation in the stratosphere.

110 The structure of the paper is as follows: After introduction the description of the used dataset  
111 and method can be found in the second section. Then we describe our results and in the last  
112 section we discuss the possible connection to previous studies.

113

## 114 **2) Data and methods**

115 The selection of streamer events is based on the visual inspection of global maps of total  
116 ozone column (TCO), accessible through a service provided by DLR  
117 (<https://atmos.eoc.dlr.de/>) measured by the Tropospheric Monitoring Instrument (TROPOMI)  
118 aboard the Sentinel 5 Precursor (S5P) mission. See Veefkind et al., 2012 for details about  
119 TROPOMI/S5P. In cases where TROPOMI/S5P data is unavailable, measurements from the  
120 Global Ozone Monitoring Experiment-2 (GOME-2) on the Metop series of satellites are  
121 utilized. Both instruments operate in a nadir-viewing configuration on near-polar sun-  
122 synchronous orbits. Further specifics regarding TCO measurements by TROPOMI/S5P are  
123 elaborated by Spurr et al. (2022). The TCO retrieval process is built upon the predecessor  
124 instrument's processor, with GOME-2 on Metop-AB, see Munro et al. (2006) and Munro et al.

125 (2016). For detailed information on the GOME-2 retrieval algorithm, refer to Loyola et al.  
126 (2011).

127 We define a streamer as such when the ozone column concentration of the finger-like  
128 structure above the Northern Atlantic/Western Europe is lower than 300 DU and persists for  
129 at least 3 days. The longitudinal extension is of approx. 15 to 30 degrees in the mid-latitudes  
130 (between 30 to 70°N). The northernmost point of a streamer exceeds 50°N. Fig. 1 shows a  
131 streamer event above the Northern Atlantic, indicated by the blue color which represent the  
132 low ozone concentrations. The streamer shown in Fig. 1 reaches latitudes beyond 70°N,  
133 which indicates a large example. At the western and eastern flanks of the streamer, the ozone  
134 concentration exceeds 350 DU, defining distinct boundaries. This is also visible in Fig. 1  
135 represented by the green colors at the eastern coast of Northern America and western Europe.  
136 So, there is a gradient of the ozone concentration of about 50 DU / 5°. Furthermore, the  
137 streamer exhibits a discernible pattern of circulation, with air masses being meridionally  
138 deflected, contributing to its formation and maintenance. These air masses, characterized by  
139 their movement from south to north at the eastern flank and from north to south at the western  
140 flank, play a significant role in the streamer's dynamics. This is the reason why equatorial low  
141 ozone concentration is transported northward. In contrast, the calm periods, representing the  
142 opposite dynamic situation to the streamer events, are characterized by only very few  
143 meridionally deflected air masses. During these periods, the ozone concentration in the mid-  
144 latitudes above the Northern Atlantic is consistently higher than 350 DU, indicating stable  
145 atmospheric conditions and minimal perturbations in the ozone distribution. An example for a  
146 calm period is shown in Fig. 2.

147 The streamer events are selected by eye for this study (results see Table 1) considering the  
148 TO3 global maps from January 2020 and March 2021. As planetary waves are permanently  
149 disturbing the atmospheric dynamic of the higher troposphere / lower stratosphere, especially  
150 smaller scale streamers can be observed almost every day and the identification of streamer  
151 events becomes subjective. We therefore focus on few events which are comparatively strong  
152 in their evolution from our perspective. Moreover, we focus on streamer events above the  
153 Northern Atlantic. Whenever another streamer event occurs somewhere other than over the  
154 Northern Atlantic region with comparable spatiotemporal extent, we do not consider this date  
155 as a streamer event. We assume that the effects of the streamer superimpose and a distinct  
156 backtrack to the streamer over the Northern Atlantic will not be possible. This means, that the  
157 analysis of the streamer events can be blurred to some extent.

158 We consider dates from January 2020 to April 2021. In general, planetary waves drive the  
 159 Brewer Dobson Circulation in the stratosphere during winter and ozone-poor airmasses are  
 160 transported northward. Streamer events are therefore detected between September and March.  
 161 The streamer events are distinguished if they have a large spatial size, high intensity (low  
 162 TO3 concentration) and if air masses are irreversibly mixed into the surrounding atmosphere.  
 163 All the selected events persist for several days, but no longer than 10 days.

164 To evaluate whether streamer events effect the smaller-scale atmospheric dynamics, calm  
 165 events are identified as well by subjective criteria. These events serve as a reference to  
 166 streamer events, as large-scale spatial structures are hardly visible in the TO3. The events are  
 167 selected when the ozone concentration shows a meridional gradient from the equator to the  
 168 polar region on the Northern Hemisphere with almost no longitudinal variation. The examples  
 169 of calm atmospheric dynamics are listed in Table 1 (right).

170

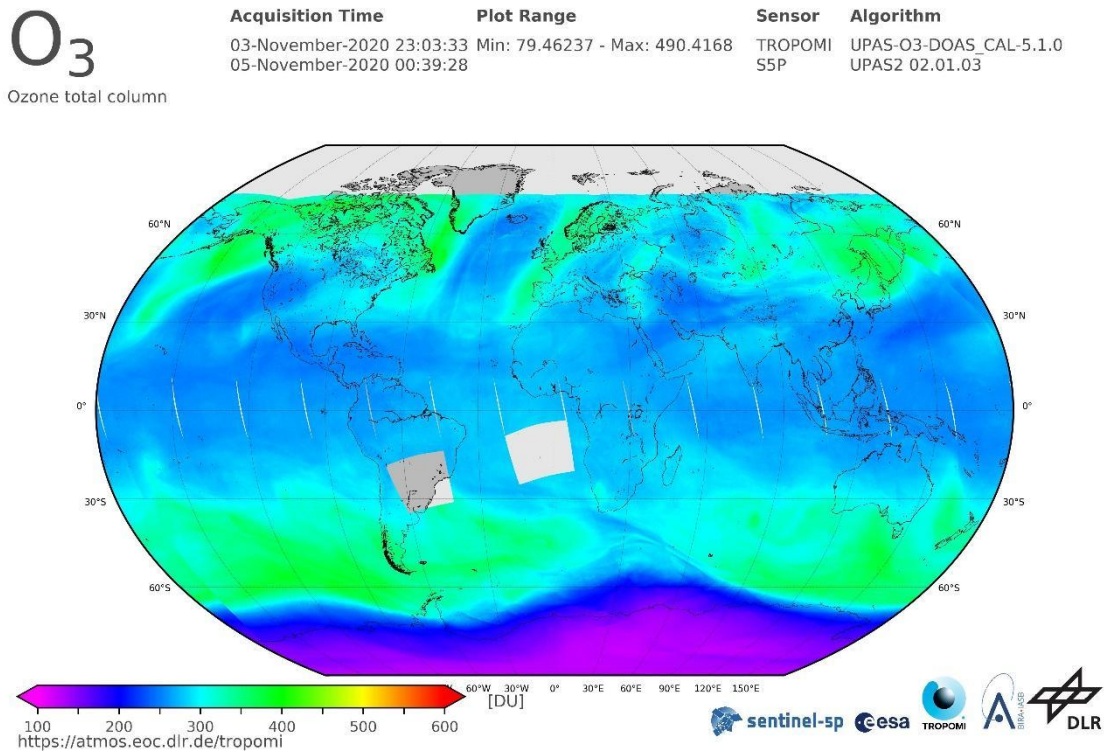
<b>Streamer events</b>		<b>Calm periods</b>	
<b>From</b>	<b>To</b>	<b>From</b>	<b>To</b>
06.02.2020	10.02.2020	02.03.2020	08.03.2020
11.2.2020	13.2.2020	09.03.2020	14.03.2020
31.08.2020	03.09.2020	28.03.2020	10.04.2020
05.09.2020	11.09.2020	19.04.2020	27.05.2020
03.11.2020	07.11.2020	9.11.2020	15.11.2020
21.11.2020	25.11.2020	12.12.2020	22.12.2020
23.02.2021	27.02.2021	30.12.2020	06.01.2021
09.03.2021	12.03.2021	21.01.2021	20.02.2021
		28.02.2021	07.03.2021
		13.03.2021	24.03.2021
		29.03.2021	07.04.2021

--	--	--	--

171 **Table 1** Streamer events above Northern Atlantic from January 2020 until March 2021 and  
 172 related start and end dates. The right part shows calm periods.

173

174 Figure 1 shows the TCO by TOPOMI/S5P integrated from November 3<sup>rd</sup> to November 5<sup>th</sup>  
 175 2020. Ozone-poor airmasses (blue) are located above the Northern Atlantic from 30°N to  
 176 70°N next to smaller scale ozone-poor airmasses above western North America and Central  
 177 Asia. The TO3 concentration is disturbed by planetary waves along the latitudes, which lead  
 178 to wave structures visible especially at the transition of blue to green colors. A large streamer  
 179 event of ozone-poor airmasses is detected over the Northern Atlantic. A small streamer can be  
 180 detected over western North America. There are also ozone-poor air masses above eastern  
 181 Europe. The temporal evolution shows, that the ozone-poor air masses above eastern Europe  
 182 are due to a decaying streamer which evolved several days earlier. As planetary waves are  
 183 more or less permanently disturbing the atmospheric dynamics, especially smaller scale  
 184 streamers can be detected almost every day. In this example, the streamer event above the  
 185 Northern Atlantic is largest. Therefore, we consider this event for the further analysis.



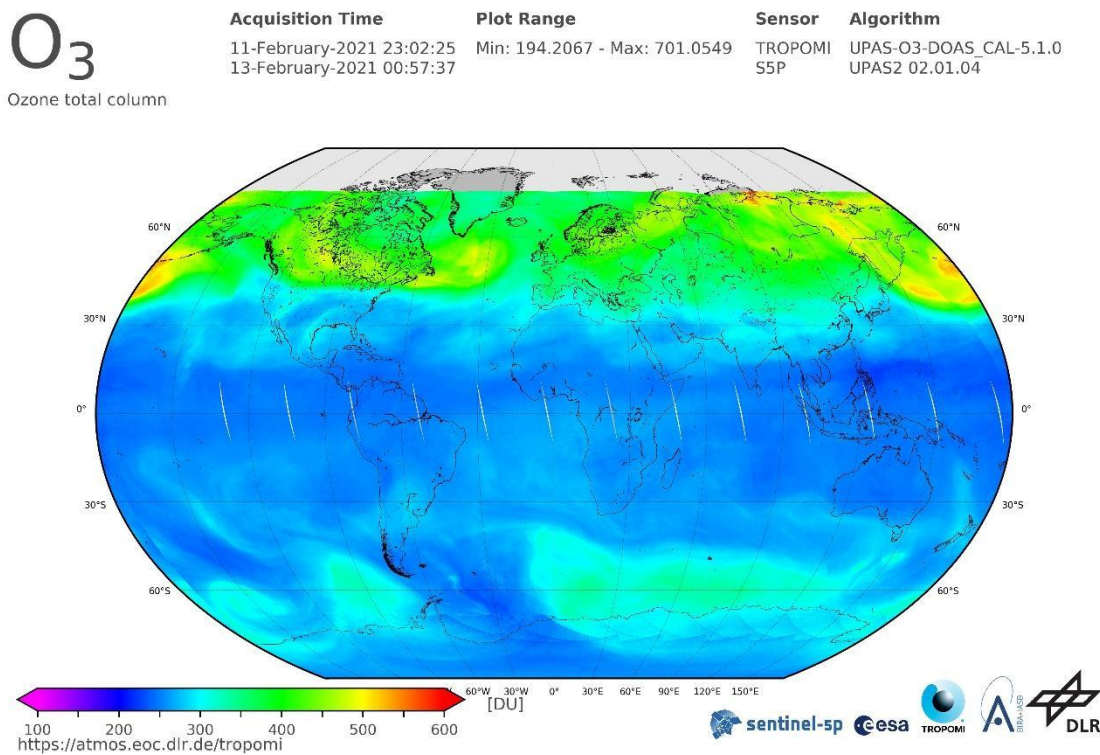


187 Fig. 1. TCO by TROPOMI/S5P from November 3<sup>rd</sup> to November 5<sup>th</sup> 2020 shows ozone poor  
 188 airmasses above the Northern Atlantic as an example of a streamer event for the further  
 189 analysis. Colors (from violet to red) indicate the total ozone column concentrations (from low  
 190 to high) in Dobson Units. Source: DLR, CC-BY 3.0

191

192 Figure 2 shows the TCO by TOPOMI/S5P from February 11<sup>th</sup> to February 13<sup>th</sup> 2020. The  
 193 event is characterized by a strong meridional gradient from the equatorial to polar region on  
 194 the Northern Hemisphere with almost no longitudinal variation. Therefore, we consider this  
 195 event for the further analysis.

196



198 Fig. 2. TCO by TROPOMI/S5P from February 11<sup>th</sup> to February 13<sup>th</sup> 2020 as an example of  
 199 calm atmospheric dynamics. A clear meridional gradient of ozone can be observed on the  
 200 Northern Hemisphere without large-scale wave structures. Colors (from violet to red) indicate  
 201 the total ozone column concentrations (from low to high) in Dobson Units. Source: DLR, CC-  
 202 BY 3.0

203 Two stations of the Czech microbarograph network (Bondar et al., 2022) are involved in the  
 204 study – the large aperture array WBCI (50.25°N 12.44°E) and the small aperture array PVICI  
 205 (50.52°N 14.57°E). To study propagation of GW and long-period infrasound (from acoustic  
 206 cut-off up to about 2.5 s) pressure recordings at WBCI are utilized. Four sensors of the WBCI  
 207 array are arranged in a tetragon. The inter-element distances of 4 – 10 km define an optimum  
 208 performance of the array in the infrasound frequency range from the acoustic cut-off



209 frequency of 0.0033 to 0.0068 Hz (Garcès, 2013). The WBCI array with its large inter-  
 210 element distances has a unique configuration compared to the arrays of the International  
 211 Monitoring System of the Comprehensive Nuclear Test Ban Treaty Organisation intended  
 212 for infrasound monitoring in the frequency band of 0.02 – 4 Hz (Marty, 2019). Each array  
 213 element at WBCI is equipped with an absolute microbarometer of the type Paroscientific  
 214 6000-16B-IS with parts-per-billion resolution. A GPS receiver is used for time stamping. Data  
 215 are stored with a sampling rate of 50 Hz. For infrasound monitoring, WBCI data are  
 216 resampled at 10 Hz sampling rate. To detect and analyze GW, 1-min mean values of the  
 217 absolute pressure data are used.

218 The small aperture array PPCI provides optimal precision of detections in the frequency  
 219 range of 0.14 – 3.4 Hz (Garcès, 2013). Three sensors are arranged in an equilateral triangle;  
 220 the array aperture is 200 m. The differential sensors of the type Infrasound Gage ISGM03  
 221 manufactured by the Scientific and Technical Centre give a flat response in the frequency  
 222 range of 0.02 – 4 Hz. A GPS receiver is used for time stamping. The data are stored with a  
 223 sampling frequency of 25 Hz. This sampling rate is also used in regular processing of  
 224 infrasound detections at PPCI.

225 Infrasound detections are processed using the DTK-GPMCC software the core of which is the  
 226 Progressive Multi-Channel Correlation (PMCC) detection algorithm (Cansi, 1995; Le Pichon  
 227 and Cansi, 2003). PMCC analyses pressure recordings from an infrasound array and looks for  
 228 coherent signals in overlapping time windows in several frequency bands (Le Pichon and  
 229 Cansi, 2003). An elementary detection with the PMCC, or the detection pixel is declared in  
 230 the time-frequency window, when signal correlation and consistency criteria are met.

231 Detection pixels are grouped into the detection families based on similar time, frequency,  
 232 azimuth of signal arrival, and signal trace velocity (Brachet et al., 2010). The arrival  
 233 parameters of the detected infrasound are stored in the detection bulletins. The parameters of  
 234 interest for the present study include time of arrival, azimuth of arrival, trace velocity,  
 235 frequency, and amplitude. The PMCC configuration is set on an individual basis and is  
 236 optimized for the given array (Brachet et al., 2010; Garcès, 2013; Szuberla et al., 2004); main  
 237 parameters of the DTK-GPMCC settings for the arrays PPCI and WBCI are given in Table 2.

Station	PPCI	WBCI
Detection range	0.09-7 Hz	0.0033-0.4 Hz
Number of detection bands	19	11

Length of the detection window; frequency dependent	412.84-6.44 s	2555-118 s
Adjacent windows overlap	95 %	90 %
Consistency	0.1 s	3 s
Azimuth tolerance for families forming	10°	3°
Family size	10-50 pixels	15-50 pixels
Frequency range analysed in the study of streamer events	0.09-0.4 Hz	0.0033-0.4 Hz

238

239 **Table 2.** Main parameters of the DTK-GPMCC configurations for the arrays PPCI and  
240 WBCI.

241

242 InfraGA/GeoAc raytracing tools are employed to study infrasound ducting in the atmosphere  
243 (Blom and Waxler, 2012; Blom, 2019). Infrasound raytracing provides an easy-to-interpret  
244 approximation of infrasound propagation and can help to identify possible modifications of  
245 atmospheric waveguides above Eastern Atlantic and Western Europe during streamer events  
246 and it can show whether the streamer event influences reach Central Europe. The raytracing is  
247 employed in our study for the purpose of identifying azimuths and distances from the source  
248 that can be influenced by the streamer event. And so, it can reveal whether these influences  
249 reach Central Europe or the signals are ducted to the region through the waveguide in the  
250 upper stratosphere or thermosphere like in quiet periods. InfraGA/GeoAc provides  
251 simulations of signal propagation from a point source; propagation through the range  
252 dependent atmosphere is modelled in the present study. Atmospheric characteristics are  
253 obtained from the G2S model (Drob et al. 2003). Vertical profiles of temperature, zonal and  
254 meridional winds, density and pressure are an input for the InfraGA/GeoAc. The grid of  
255 profiles covers the area from 45° to 65°N and from 30°W to 22.5°E; latitudinal step is 5° and  
256 longitudinal step is 7.5°.

257 Propagation of GW in the thermosphere/ionosphere is studied using the multi-point and multi-  
258 frequency continuous Doppler sounding system located in Czechia. Its advantage is a high  
259 time resolution (around 10 s) compared with ionospheric sounders (ionosondes) that measure  
260 the profile of electron densities in the ionosphere. The frequency shift is due to the motion and  
261 electron density changes in the ionospheric plasma, caused for example by interaction with

262 atmospheric waves propagating in the neutral atmosphere, with which the ionosphere (above  
263 ~ 80 km) merges. The sounding radio signal is reflected at the height, where its frequency  
264 matches the so called local plasma frequency, which is determined by the local electron  
265 density. Therefore, the reflection height changes during the day and depends on the sounding  
266 frequency. Significant Doppler shifts, usable for analysis, are obtained if the signal is  
267 reflected from the so called ionospheric F2 layer (approximately 200 – 300 km). Several  
268 sounding frequencies are used in Czechia. The 3.59 MHz sounding was mostly effective at  
269 night, while the 4.65 MHz sounding provided good daytime data during the period analyzed.  
270 The propagation characteristics of GWs are calculated from the time delays between signals  
271 observed at the respective sounding paths (reflection points for each transmitter-receiver  
272 pairs) assuming that the reflection points are in the midpoints between each transmitter and  
273 receiver. A 60 or 90 min long time interval is usually used to calculate the velocities and  
274 azimuth of the observed waves. The methods are in detail described by Chum and Podolska  
275 (2018). The two-dimensional (2-D) version (propagation analysis in horizontal plane only) is  
276 anticipated for most of the studies, since a 3-D analysis requires simultaneous observation and  
277 signal correlation at different frequencies, which is often not the case, especially during solar  
278 minimum. Results of statistical investigation have been recently published (Chum et al.,  
279 2021). Identical methods of propagation analysis have been applied to investigate  
280 propagation of GWs in the troposphere based on data from large-aperture array WBCI (here  
281 the time delays are related to the locations of individual microbarometers). All analyses will  
282 be done with respect to the streamer events and calm periods shown in Table 1.

### 283 **3) Results**

#### 284 **3.1 Infrasound observations at ground microbarograph arrays WBCI and PPCI in** 285 **November 2020 and in March 2021**

286 Wave activity in the infrasound frequency range of 0.0033-0.4 Hz is investigated combining  
287 observations at the stations WBCI and PPCI. Infrasound detections at WBCI are processed in  
288 the frequency band of 0.0033 – 0.4 Hz. The operational range of the array is extended above  
289 the upper limit of the optimum array range; the degraded performance of WBCI at  
290 frequencies higher than 0.0068 Hz shall be considered. The upper limit of the analysed band  
291 is intentionally set to 0.4 Hz to cover microbaroms. PPCI detections are analysed in the  
292 frequency range of 0.09 – 0.4 Hz. The band partly overlaps with the detection range of the  
293 WBCI array and at frequencies of 0.12 – 0.35 Hz it is dominated by microbaroms (e.g.,

294 Campus and Christie, 2010). Unlike WBCI, PPCI provides an optimal performance in the  
295 microbarom band.

296 Microbaroms are infrasound signals generated by a non-linear interaction of ocean waves  
297 travelling in opposite directions. Microbaroms form a wide peak around 0.2 Hz in the  
298 infrasound spectrum; their frequency corresponds to twice the frequency of sea waves. A  
299 powerful source of microbaroms is located in the North Atlantic and the signals are regularly  
300 detected by European stations (Hupe et al., 2019). The detection capability of microbaroms  
301 from the North Atlantic is particularly high from October to March when the source becomes  
302 stronger due to stormy weather above the ocean and signal propagation to the East from the  
303 source is supported by the stratospheric waveguide (Landès et al., 2012). From the global  
304 point of view, microbaroms are permanently present in recordings of infrasound stations  
305 worldwide.

306 Streamer events often occur above the North Atlantic. Thus, microbaroms propagating from  
307 the North Atlantic to the continental Europe can travel through the region influenced by a  
308 streamer event and the detections at infrasound stations in Europe can show signatures of  
309 streamer events.

310 We analyse infrasound observations from 3<sup>rd</sup> to 25<sup>th</sup> November 2020 and from 28<sup>th</sup>  
311 February to 25<sup>th</sup> March 2021 with focus on microbaroms. In these time intervals adjacent  
312 streamers and calm periods occurred (Table 1). Streamer events and the calm period in the  
313 November 2020 time window are evaluated separately from those in the March 2021 time  
314 window to avoid seasonal influences. While a well-developed eastward stratospheric  
315 waveguide can be expected in November, its efficiency can decrease in March due to the  
316 seasonal reversal of stratospheric winds.

317

### 318 **3.1.1 Infrasound observations from 3<sup>rd</sup> to 25<sup>th</sup> November 2020**

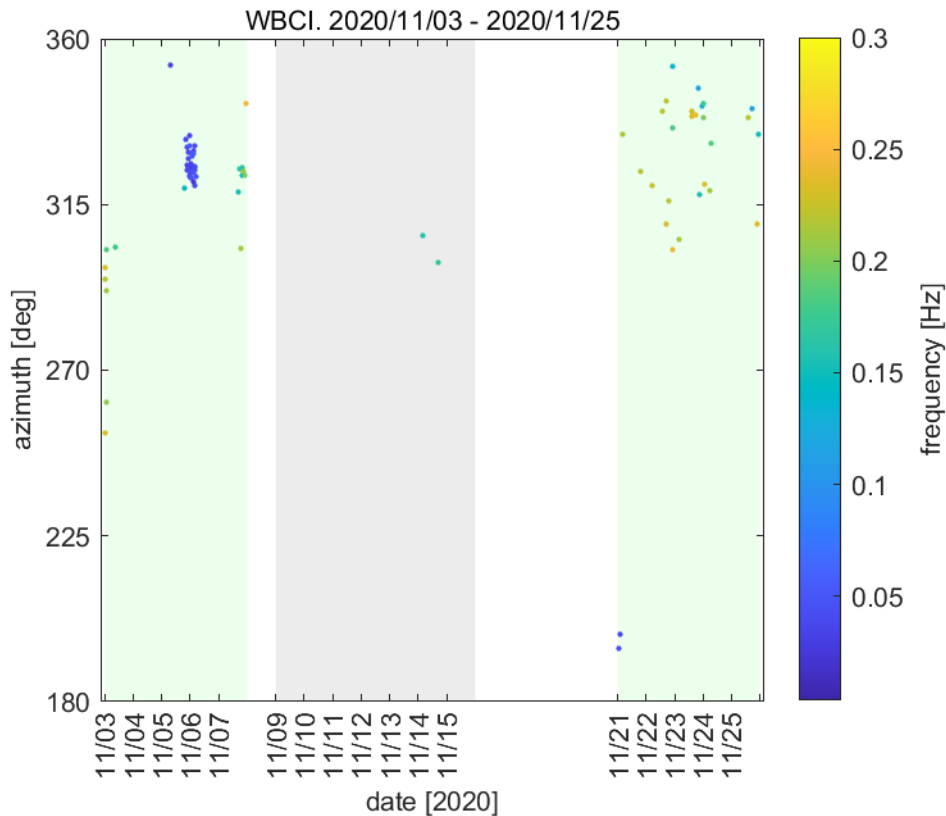
319 Two streamer events developed in November 2020. The first streamer occurred from 3<sup>rd</sup>  
320 to 7<sup>th</sup> November and the second one from 21<sup>st</sup> to 25<sup>th</sup> November. The streamers were  
321 separated by a calm period from 9<sup>th</sup> to 15<sup>th</sup> November.

322 The most important phenomena found in the infrasound arrival parameters are fluctuating  
323 signal frequency and fluctuating signal amplitude.

324 WBCI provides rather sparse detections during both streamer events and only two  
325 detection families are obtained during the seven-day calm period (Figure 3). The  
326 frequencies near 0.2 Hz and back-azimuths of 290° – 350° indicate that the observed  
327 signals are likely microbaroms from the North Atlantic. A decrease of the signal frequency

328 is observed during the first streamer event. On 5<sup>th</sup> – 6<sup>th</sup> November from 20 to 05 UTC, the  
 329 mean frequency of the north-west arrivals drops down to 0.04 Hz, below the microbarom  
 330 frequency range. During the second streamer event from 21<sup>st</sup> to 25<sup>th</sup> November, the signal  
 331 frequency is stable around 0.22 Hz. An increase of the amplitude from the mean value of  
 332 0.019 Pa to 0.035 Pa is observed from 23<sup>rd</sup> November, 18 UTC until the end of the analysed  
 333 time period on 25<sup>th</sup> November at 24 UTC.

334



335

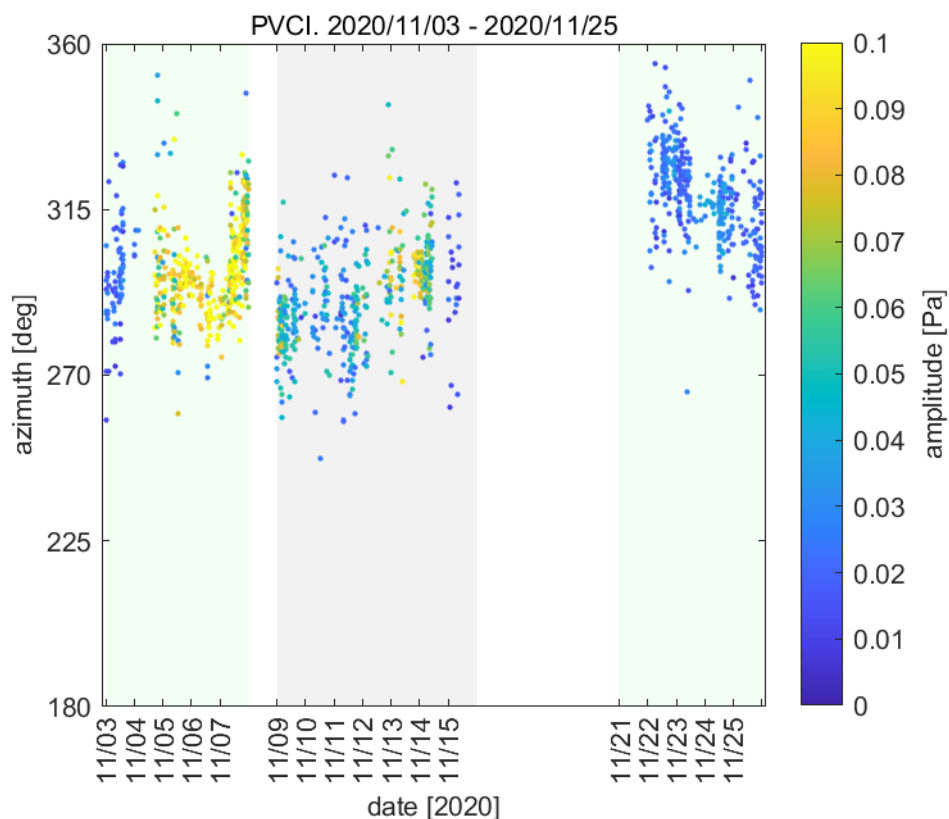
336 Fig. 3. Infrasound observations at WBCI on 3<sup>rd</sup> - 25<sup>th</sup> November 2020. Azimuth of signal  
 337 arrivals is shown; the colorbar refers to the mean frequency of the detection family. One circle  
 338 in the plot represents one detection family. Green background marks the streamer events, grey  
 339 background marks the calm period.

340

341 Similar to the back-azimuths at WBCI, PSCI detects arrivals from the north-west in the  
 342 analysed frequency range of 0.09 – 0.4 Hz (Figure 4). Fluctuating signal amplitudes are  
 343 observed. Values around 0.020 Pa occur on 3<sup>rd</sup> November. From 4<sup>th</sup> November, 18 UTC to 7<sup>th</sup>  
 344 November, 22:30 UTC, the signals are of amplitudes around 0.089 Pa. The amplitudes  
 345 decrease to the values around 0.046 Pa during the following quiet period on 9<sup>th</sup> – 15<sup>th</sup>  
 346 November. Microbarom amplitudes fluctuate between 0.013 and 0.036 Pa (1<sup>st</sup> decile and 9<sup>th</sup>

347 decile, respectively) during the streamer event on 21<sup>st</sup> – 25<sup>th</sup> November. Publicly available  
 348 data such as meteorological charts provided by Deutscher Wetterdienst and the  
 349 WAVEWATCHIII® wave-action model (The WAVEWATCHIII® Development Group,  
 350 2016) indicate that there are maritime storms in the North Atlantic within the analysed time  
 351 window from 3<sup>rd</sup> to 25<sup>th</sup> November 2020. Maximum heights of sea waves are predicted in the  
 352 North Atlantic near south coast of Greenland and Island from 5<sup>th</sup> to 6<sup>th</sup> November, from 12<sup>th</sup>  
 353 to 13<sup>th</sup> November, and on 20<sup>th</sup> November. The height of combined wind waves and swell  
 354 reaches 10 m. As mentioned in section 3.1 it is not only the wave height but also the wave  
 355 direction (waves propagating in opposite directions) that determines the microbarom source.  
 356 Nevertheless, fluctuating intensity of the microbarom source shall be taken into account  
 357 during maritime storms. As a consequence, fluctuating microbarom amplitudes can be  
 358 observed at the infrasound stations.

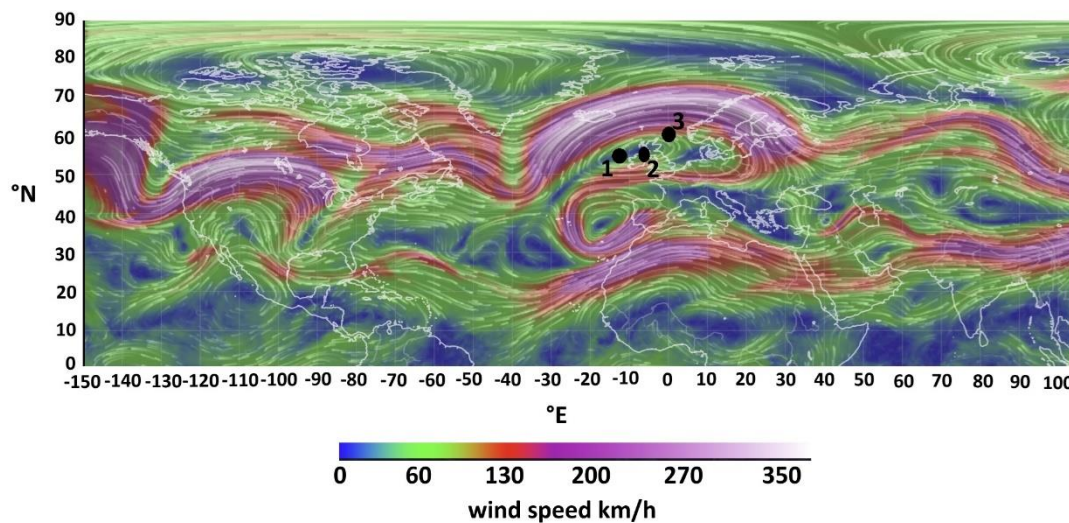
359  
 360  
 361



362  
 363 Fig.4. Infrasound observations at PVC I on 3<sup>rd</sup> - 25<sup>th</sup> November 2020. Azimuth of signal  
 364 arrival is shown; the colorbar refers to the signal amplitude. Green background marks the  
 365 streamer events, grey background marks the calm period.

366

367 To study propagation of signals from sources located at the surface of the North Atlantic  
368 the InfraGA/GeoAc tools are employed. The fictitious point sources are located (1) at 55°N  
369 and 15°W, (2) at 55°N and 5°W, and (3) at 60°N and 0°longitude. The coordinates of the  
370 sources are estimated based on the position of the tropopause jet stream disturbance. Point  
371 (1) is located under the northward jet-stream, point (3) under the southward jet-stream, and  
372 point (2) is located between those two opposing branches of the jet stream disturbance, see  
373 Figure 5.



374

375

376 Fig.5. Wind field at the pressure level of 250 hPa on 06 November 2020 at 00 UTC. A  
377 disturbance of the jet-stream above the eastern North Atlantic and the British Isles is caused  
378 by the streamer event. Figure taken from [earth.nullschool.net](http://earth.nullschool.net)

379

380 A multi azimuth simulation is run on 6th November at 00 UTC. The simulation is performed  
381 at the time point in the middle of the streamer event when a maximum stage of the  
382 phenomenon can be expected. Taking into account the mutual locations of the sources and the  
383 receiving arrays, eastward signal propagation is modelled. The azimuth limits are set to 0° and  
384 180°, the azimuth step is 3°. Rays are launched with inclinations of 2° - 45°; the step is 2°.  
385 Information is obtained through which waveguides the signal can possibly arrive to the  
386 infrasound stations and their surroundings. The reason why arrivals **to extended areas around**  
387 **the stations** are considered is that signal propagation from three fictitious point sources stands  
388 in for a real source, the surface of the North Atlantic where microbaroms are generated.  
389 Therefore, the model outputs must be taken as an approximation of the real situation. The



390 turning height and ground reflections of the 0.2 Hz signal are obtained in the multi azimuth  
391 simulation. The results are visualised in Figure 6 and in supplementary materials. The red  
392 asterisk represents the point source. The concentric sectors of circles show i.e. regions of  
393 ensonification, regions where the signal emitted by the source can be recorded at an  
394 infrasound station. The dots showing signal ground reflections are organized in a radial  
395 pattern. Each of the lines of this pattern represents one azimuth of signal propagation for  
396 which the multi azimuth simulation is run; the azimuth step is  $3^\circ$ . The colours of the dots  
397 inform about the turning height of the ray and thus provide information about signal ducting  
398 in the waveguides. Depending on the turning height, infrasound is subject to attenuation of  
399 variable strength when it propagates through the atmosphere. Infrasound attenuation is low in  
400 the stratospheric waveguide. Strong absorption occurs in the thermospheric waveguide; the  
401 absorption is higher at higher signal frequencies (Sutherland and Bass, 2004). To obtain the  
402 view of signal attenuation along the raypath in the vertical plain a single azimuth simulation  
403 is employed. The single azimuth simulation is run along the azimuths from the fictitious  
404 sources (1) – (3) to the stations WBCI and PPCI; it is obtained for the frequencies of 0.04 Hz  
405 and 0.2 Hz. As a reference, a multi azimuth propagation of the 0.2 Hz signal is modelled from  
406 a source at  $55^\circ\text{N}$  and  $15^\circ\text{W}$  on the calm day 12<sup>th</sup> November at 00 UTC. The time point in the  
407 middle of the calm period between two streamer events is selected to minimize possible  
408 effects of the subsiding and arising streamer event, respectively.

409 First, we focus on infrasound propagation from the North Atlantic to Central Europe. Signal  
410 arrivals only through the thermospheric waveguide are enabled from the source at  $60^\circ\text{N}$  and  
411  $0^\circ$  longitude (Figure 6) during the streamer event on 6<sup>th</sup> November 2020 at 00 UTC.

412 Stratospheric and thermospheric ducting are possible from the sources at  $55^\circ\text{N}$   $15^\circ\text{W}$  and  
413  $55^\circ\text{N}$   $5^\circ\text{W}$  to Central Europe (supplementary materials). Similarly, stratospheric and  
414 thermospheric ducting is predicted from the source at  $55^\circ\text{N}$   $15^\circ\text{W}$  to Central Europe on the  
415 calm day 12<sup>th</sup> November 2020 (supplementary materials). Signal propagation only through the  
416 thermospheric waveguide is enabled from the source at  $60^\circ\text{N}$  and  $0^\circ$  longitude (Figure 6). The  
417 distances between the fictitious sources and the stations are 1300 – 2000 km. The amplitude  
418 loss of the 0.2 Hz signal in the thermospheric waveguide at these distances is 100 dB relative  
419 to the amplitude at a distance of 1 km from the source. According to the simulations,  
420 observations of the thermospheric arrivals of microbaroms are unlikely at PPCI and WBCI  
421 due to strong signal attenuation. Microbaroms apparently arrive to Central Europe through the  
422 stratospheric waveguide formed in the upper stratosphere during the streamer events as well  
423 as on the calm day. Indeed, arrivals from the back-azimuths of  $285^\circ$  -  $315^\circ$  are dominant at

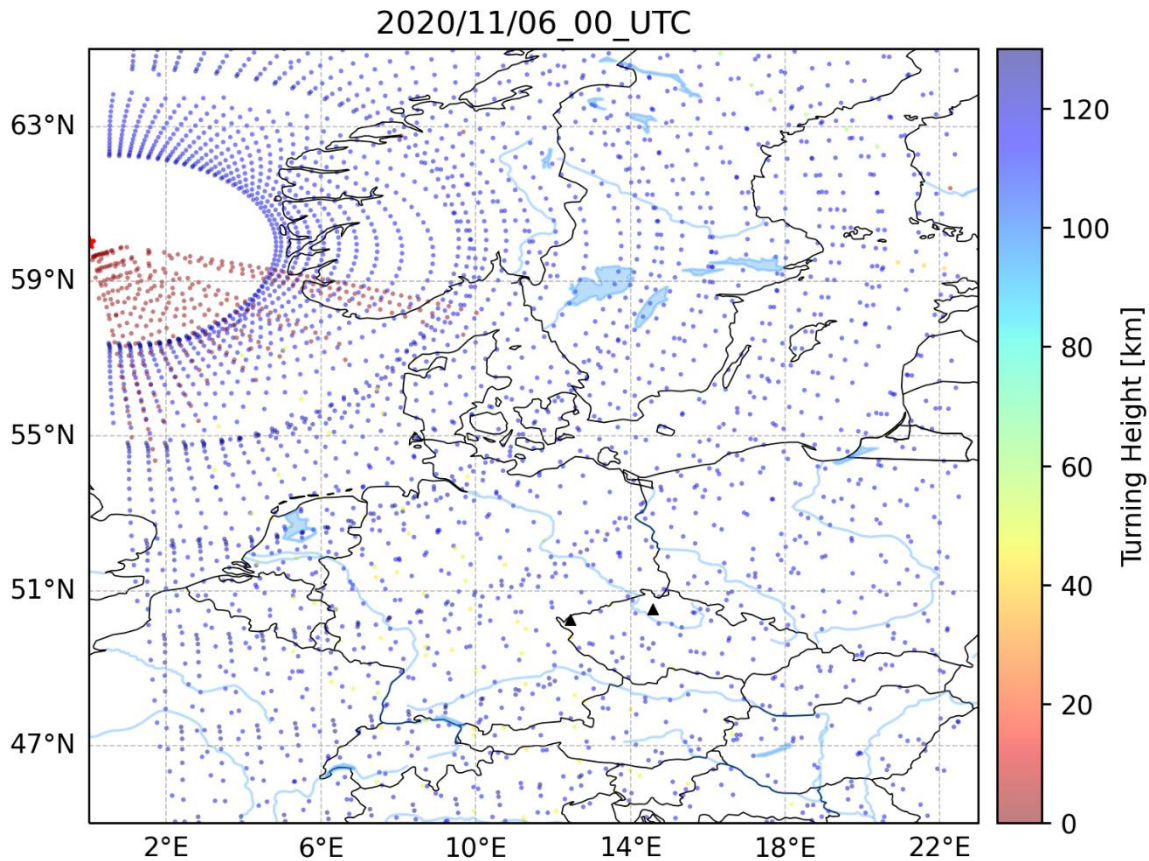
424 P/CI from 3<sup>rd</sup> to 7<sup>th</sup> November. Those back-azimuths correspond to the positions of the  
425 fictitious sources at 55°N 15°W and at 55°N 5°W, while the back-azimuth to the source at  
426 60°N and 0°latitude is 325°. The amplitude loss of the 0.04 Hz signal at the distances of 1300  
427 – 2000 km from the source is 60 – 80 dB. In general, thermospheric arrivals of this low  
428 frequency signal are not strictly rejected. However, in our case the 0.04 Hz signal arrives with  
429 trace velocity around 0.330 km/s at W/CI. The low trace velocity indicates signal  
430 propagation in the troposphere/lower stratosphere waveguide (Lonzaga, 2015).

431 Next, we study the influences of the streamer event related disturbance anywhere in the  
432 modelled region. The disturbance of the jet stream can modify signal propagation up to  
433 distances of several hundreds to a thousand km from the source; the influenced azimuth  
434 range is limited. Signals from the source at 55°N and 15°W can propagate in the tropopause  
435 waveguide in azimuths between 10° and 60° up to the distance of ~1000 km. The amplitude  
436 loss of the 0.2 Hz signal at a distance of 1000 km is 60-70 dB relative to the amplitude at 1  
437 km from the source. The southward branch of the jet-stream disturbance enables infrasound  
438 propagation in the tropospheric waveguide in azimuths of 100 - 160° from the source at  
439 60°N 0°longitude. Maximum distance which the signal can travel in the south-east direction  
440 is ~600 km. The amplitude loss of the 0.2 Hz signal at a distance of 600 km is 60 dB  
441 relative to the amplitude at 1 km from the source.

442 The observations and the model outputs during the November 2020 event can be  
443 summarized as follows: infrasound arrives from sources in the North Atlantic to Central  
444 Europe mainly through the stratospheric waveguide formed between the ground and upper  
445 stratosphere. The jet-stream disturbance above the eastern North Atlantic does not have an  
446 impact on infrasound arrivals in Central Europe on 6<sup>th</sup> November 2020 at 00 UTC.

447 Fluctuating signal amplitudes are likely a consequence of fluctuating intensity of the  
448 microbarom source during maritime storms. The decrease of signal frequency at W/CI is  
449 not caused by a transient change in signal ducting and by the related signal filtering in the  
450 thermospheric waveguide.

451



452  
 453 Fig.6. Modelled infrasound propagation from a point source located at 60°N and 0°longitude  
 454 (red asterisk) during the streamer event on 6<sup>th</sup> November 2020 at 00 UTC. The colorbar  
 455 refers to the turning height (maximum height) of the signal. Red color indicates signal  
 456 propagation in the waveguide formed near the tropopause (altitudes around 10 km), arrivals  
 457 through the thermospheric waveguide are shown in blue (altitudes above 100 km). Black  
 458 triangles represent infrasound arrays WBCI (the left triangle) and PVICI (the right triangle).  
 459

### 460 3.1.2 Infrasound observations from 28<sup>th</sup> February to 24<sup>th</sup> March 2021

461 Another streamer event occurred from 9<sup>th</sup> to 12<sup>th</sup> March 2021 preceded and followed by  
 462 calm periods from 28<sup>th</sup> February to 7<sup>th</sup> March and from 13<sup>th</sup> to 24<sup>th</sup> March, respectively.

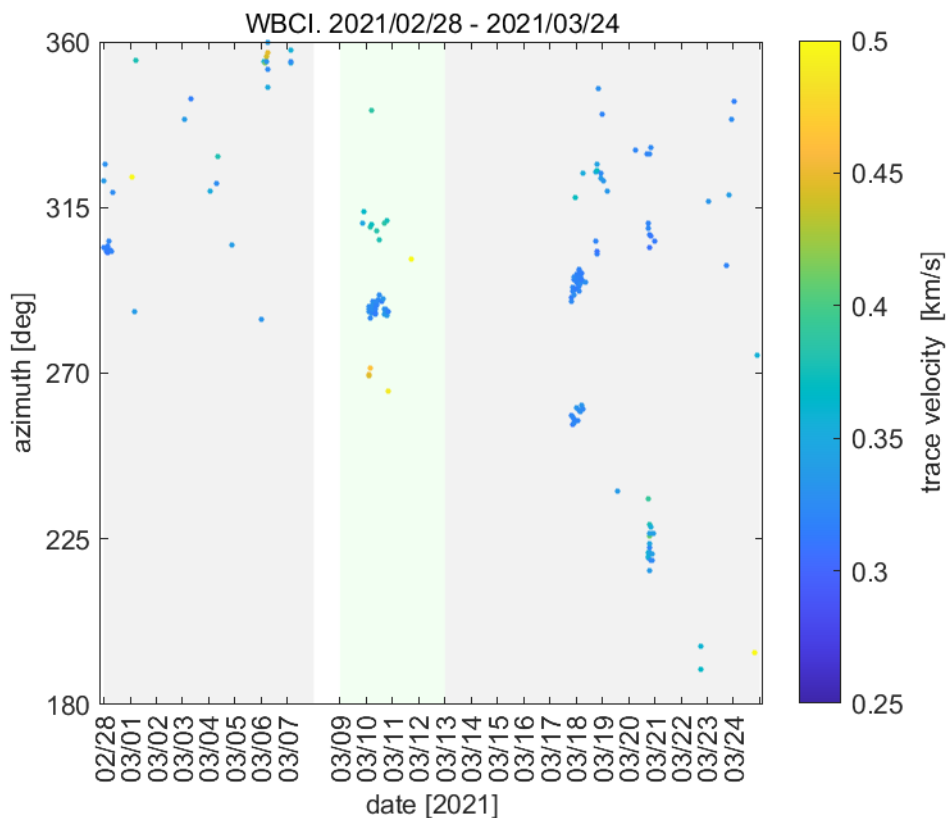
463 The most important phenomenon identified in the infrasound arrival parameters is a  
 464 fluctuating trace velocity.

465 Both WBCI and PVICI detect signals arriving from the north-west, from back-azimuths of  
 466 285° – 310°. An increase of signal trace velocities is observed in some of the detections at  
 467 WBCI during the streamer event compared to calm periods (Figure 7). On 10<sup>th</sup> March at 00 –  
 468 06 UTC, trace velocities of 0.460 km/s and 0.380 km/s are observed from back-azimuths of  
 469 270° and 310° respectively. It is by 0.05 – 0.13 km/s higher than on the calm days. On the

470 other hand, signals from the back-azimuth of  $288^\circ$  arrive with the trace velocity of 0.330 km/s  
 471 within the same time window, this velocity corresponds to that on the calm days. Effects of  
 472 spatial aliasing shall be taken into account when evaluating the detections. The signal  
 473 frequencies are around 0.2 Hz, well above the range of array optimum performance. The  
 474 observed different trace velocities at WBCI can therefore be a processing bias rather than a  
 475 consequence of variations in signal ducting.

476 In contrast to the WBCI observations, PPCI records a decrease in trace velocities on 10<sup>th</sup>  
 477 March at 00 – 06 UTC (Figure 8). Trace velocities of 0.377 km/s are observed compared to  
 478 0.413 km/s and 0.395 km/s during the calm periods before and after the streamer,  
 479 respectively.

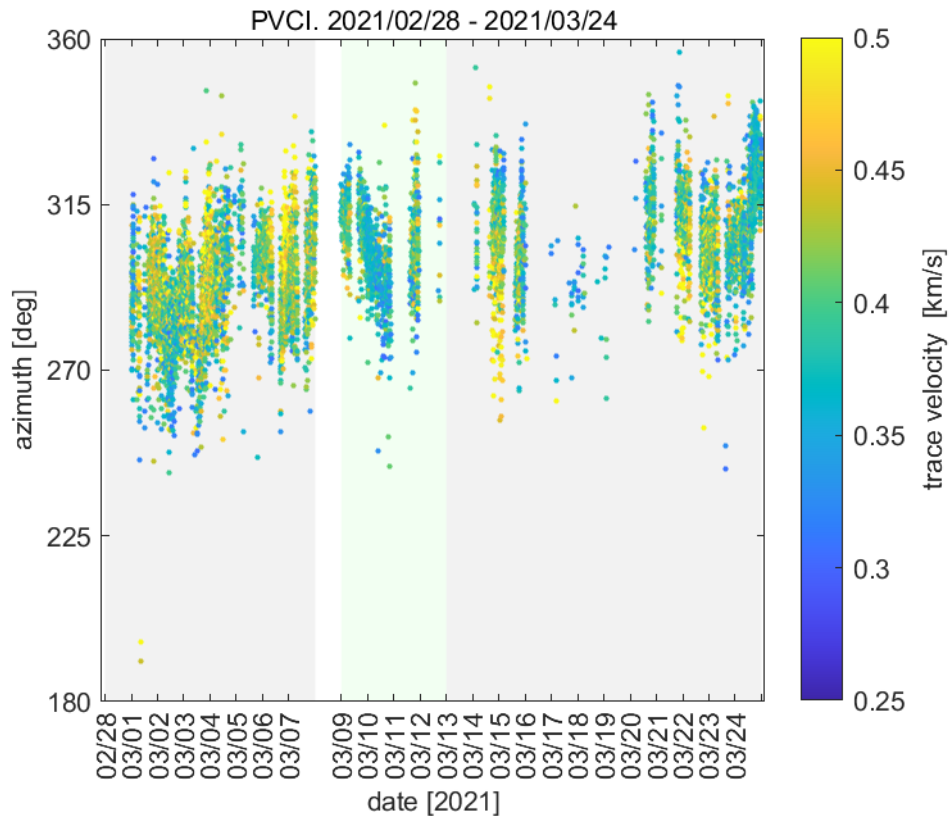
480



481

482 Fig.7. Infrasound observations at WBCI on 28<sup>th</sup> February – 24<sup>th</sup> March 2021. Azimuth of  
 483 signal arrival is shown; the colorbar refers to the signal trace velocity. Green background  
 484 marks the streamer event, grey background marks the calm periods.

485



486

487 Fig.8. Infrasound observations at PVCi on 28<sup>th</sup> February – 24<sup>th</sup> March 2021. Azimuth of  
 488 signal arrival is shown; the colorbar refers to the signal trace velocity. Green background  
 489 marks the streamer event, grey background marks the calm periods.

490

491 Changes of the trace velocity can indicate changes of the refraction altitude of the signal  
 492 (Lonzaga, 2015). The exact limits of the trace velocity for the given atmospheric waveguide  
 493 depend on the current state of the atmosphere. We use the thresholds determined for a  
 494 model atmosphere in Lonzaga (2015) as helpful hints for our further consideration: Trace  
 495 velocities below 0.340 km/s indicate signal refraction in the troposphere and lower  
 496 stratosphere. Trace velocities between 0.340 and 0.380 km/s are typical for signals ducted  
 497 in the waveguide between the ground and the upper stratosphere. Signals traveling in the  
 498 thermospheric waveguide arrive with trace velocities larger than 0.380 km/s.

499 The high trace velocities recorded at PVCi disprove signal refraction in the lower  
 500 stratosphere. Hence, it is unlikely that the signals arrive through a waveguide that can form  
 501 at the tropopause – lower stratosphere by the effect of the streamer event.

502 Like in the November 2020 case, signal propagation above the eastern North Atlantic and  
 503 Western and Central Europe is investigated using the InfraGA/GeoAc tools. Propagation of  
 504 the 0.2 Hz signal is modelled for 10<sup>th</sup> March at 03 UTC, in the middle of the streamer

505 event. A source is located at 55°N 15°W at a distance of ~2000 km from the stations. This  
506 scenario represents signal propagation from the central North Atlantic. The other source is  
507 located at 55°N 0°latitude representing propagation of microbaroms from the North Sea.  
508 The distance from the stations is ~1000 km. Both points are located under the jet-stream  
509 disturbance related to a streamer event.

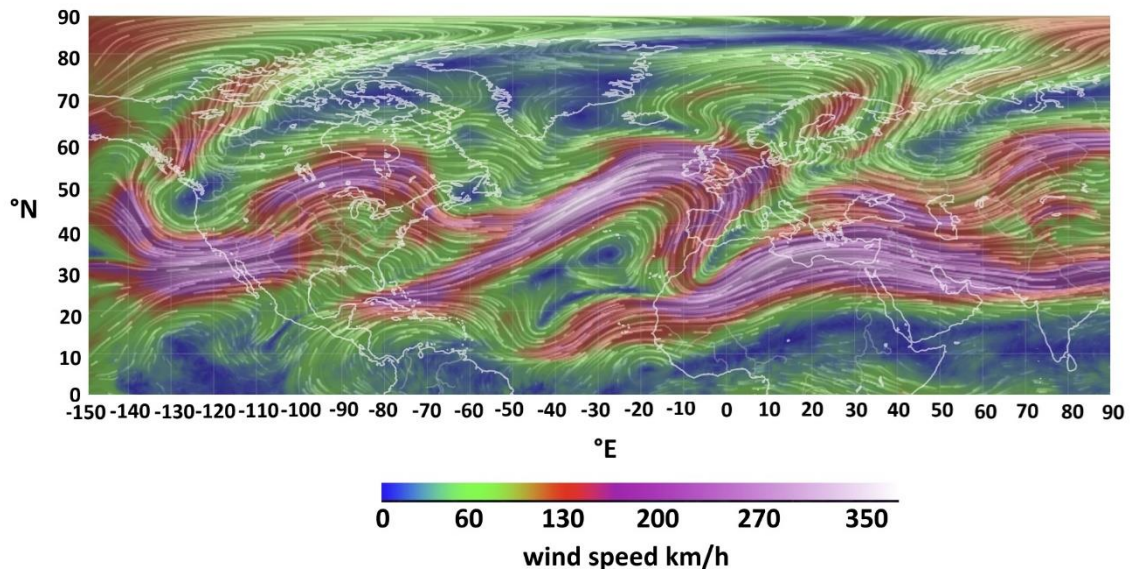
510 Eastward signal ducting is enabled in the stratospheric and thermospheric waveguides  
511 from both sources to the stations. Strong signal absorption in the thermospheric waveguide  
512 likely disables thermospheric arrivals to the PPCI and WBCI. We assume that signals  
513 ducted in the upper stratosphere are detected. The other eastward waveguide occurs near  
514 the tropopause, formed by the eastward to south-eastward jet-stream above the eastern  
515 North Atlantic and Western Europe at latitudes 50 – 60°N (Figure 9). Signals from the  
516 source in the North Atlantic are predicted to travel in the tropopause waveguide to distances  
517 of 1000-1100 km. The signal attenuation is low in the tropopause waveguide; the relatively  
518 short distance under the waveguide influence is determined by the location and extent of  
519 the jet-stream disturbance. The tropopause/lower stratosphere arrivals can be detected  
520 mainly on the British Isles. The waveguide does not reach to PPCI and WBCI stations (see  
521 supplementary materials).

522 Signals emitted by a source in the North Sea can propagate through the tropopause  
523 waveguide. The signals propagate to the south-east and are predicted to reach Central  
524 Europe. The tropopause/lower stratosphere arrivals are represented by red dots in Figure  
525 10. The influenced regions are to the south-west from PPCI and WBCI, several hundreds  
526 of kilometres distant from the stations. The approximation of infrasound propagation  
527 obtained from the raytracing is in accord with observations. The trace velocities at PPCI of  
528 0.377 km/s indicate infrasound propagation in the waveguide formed between the ground  
529 and the upper stratosphere rather than in the waveguide near the tropopause.

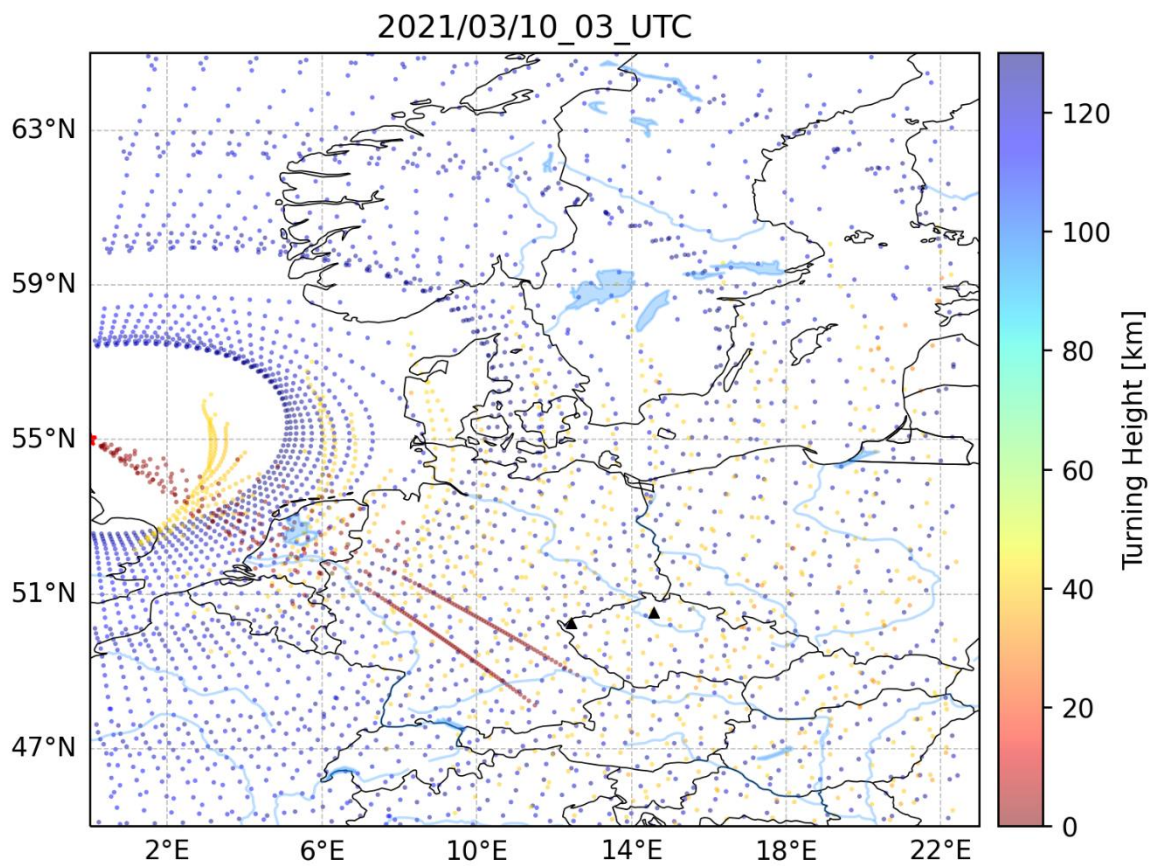
530 Like in the November 2020 case, infrasound arrivals from the North Atlantic to the  
531 stations PPCI and WBCI in Central Europe are not influenced by the waveguide at the  
532 tropopause – lower stratosphere. Observed trace velocities fluctuate within or close above  
533 the limits that indicate infrasound propagation in the upper stratosphere during the streamer  
534 event and both adjacent quiet periods.

535





536  
 537 Fig.9. Wind field at the pressure level of 250 hPa on 10 March 2021 at 03 UTC. A  
 538 disturbance of the jet-stream above the eastern North Atlantic and the British Isles is caused  
 539 by the streamer event. Figure taken from [earth.nullschool.net](http://earth.nullschool.net)  
 540



541  
 542 Fig.10 Modelled infrasound propagation from a point source located at 55°N and 0°longitude  
 543 (red asterisk) on 10<sup>th</sup> March 2021 at 03 UTC. The colorbar refers to the turning height



544 (maximum height) of the signal. Red color indicates signal propagation in the waveguide  
545 formed near the tropopause (altitudes around 10 km), arrivals through the stratospheric  
546 waveguide are shown in yellow (altitudes around 40-50 km) and arrivals through the  
547 thermospheric waveguide are shown in blue (altitudes above 100 km). Black triangles  
548 represent infrasound arrays WBCI (the left triangle) and PPCI (the right triangle).

549

550

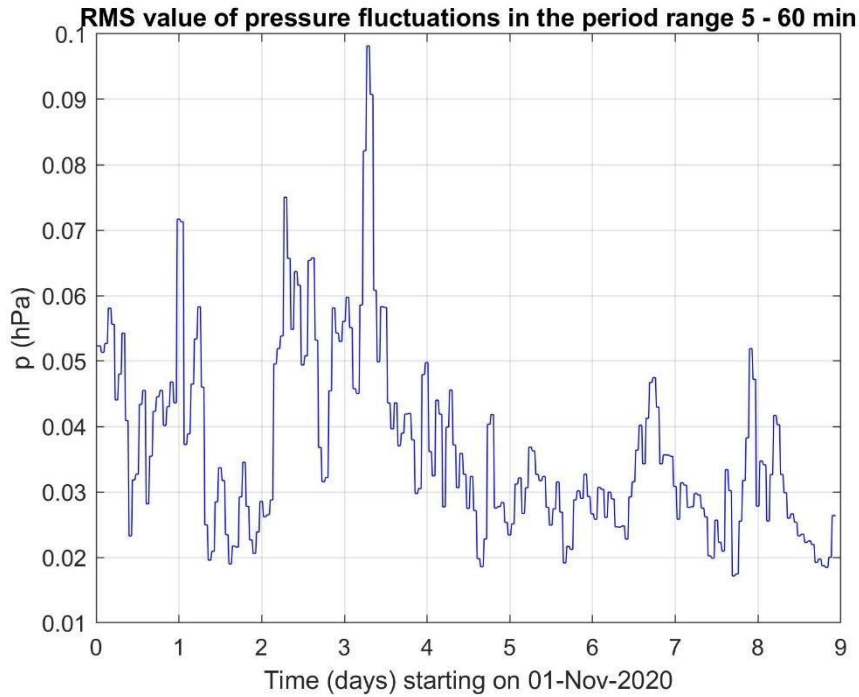
## 551 **3.2 Results and discussion of gravity waves in the troposphere and ionosphere**

552

### 553 **3.2.1 Investigation of GWs measured on the ground by WBCI array of micro-** 554 **barometers.**

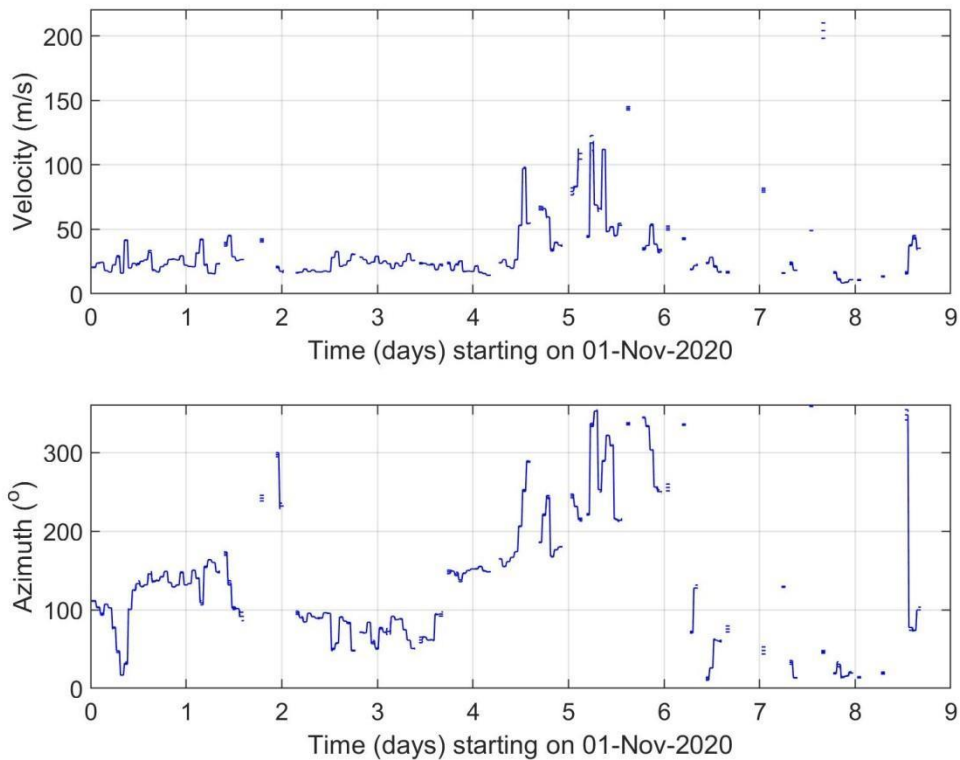
555 Figure 11 shows the RMS amplitudes of pressure fluctuations in the period range 5-60 min  
556 recorded from November 1 to November 9, 2020. This interval covers a distinct streamer  
557 event that occurred from November 3 to November 7. The results of propagation analysis are  
558 shown in Figure 12, which displays the phase velocities and azimuths of GWs. Only results  
559 that satisfied the criterion ( $dv/v < 0.5$ ) and ( $dAZ < 10^\circ$ ) and ( $p_{RMS} > 0.02$  Pa) are presented,  
560 where  $dv/v$ ,  $dAZ$ ,  $p_{RMS}$  are the relative uncertainty of GW phase velocity, uncertainty of  
561 azimuth and root mean square value of pressure fluctuations in the analysed time interval.  
562 Figure 12 demonstrates that there is a tendency for higher phase velocities and occurrence of  
563 different azimuths during the streamer event. Therefore, it is useful to compare the GW  
564 characteristics during streamer events and calm conditions.

565 Figure 13 shows histograms obtained by a statistical analysis. The RMS amplitudes of  
566 pressure fluctuations in the period range 5 – 60 min, phase velocities and azimuths were  
567 investigated separately for calm conditions (upper plots) and for streamer events listed in  
568 Table 1 (bottom plots) with a 1-hour time resolution. The solid vertical lines mark lower (Q1)  
569 and upper (Q3) quartiles. The dashed vertical lines depict boundaries for large ( $Q3 + 1.5 \cdot (Q3 -$   
570  $Q1)$ ) and extreme ( $Q3 + 3 \cdot (Q3 - Q1)$ ) values. A difference between histograms for RMS  
571 pressure fluctuations and azimuths obtained for calm and disturbed conditions is obvious.  
572 During the streamer events the azimuths are distributed more randomly and more extreme  
573 pressure amplitudes can be observed. A minor difference is also observed for phase  
574 velocities.



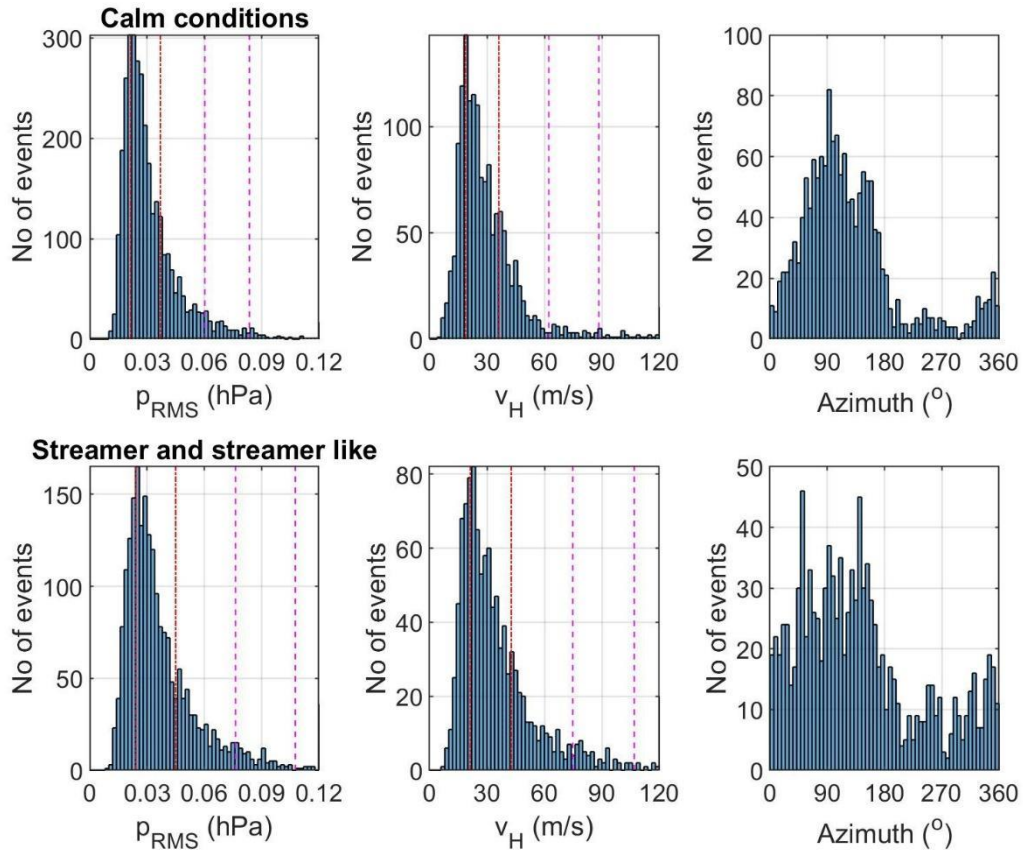
575

576 **Figure 11** Amplitude of GWs recorded by WBCI from 2020-11-01 to 2020-11-09



577

578 **Figure 12** Propagation velocity and azimuth of GWs recorded by WBCI from 2020-11-01 to  
 579 2020-11-09



580

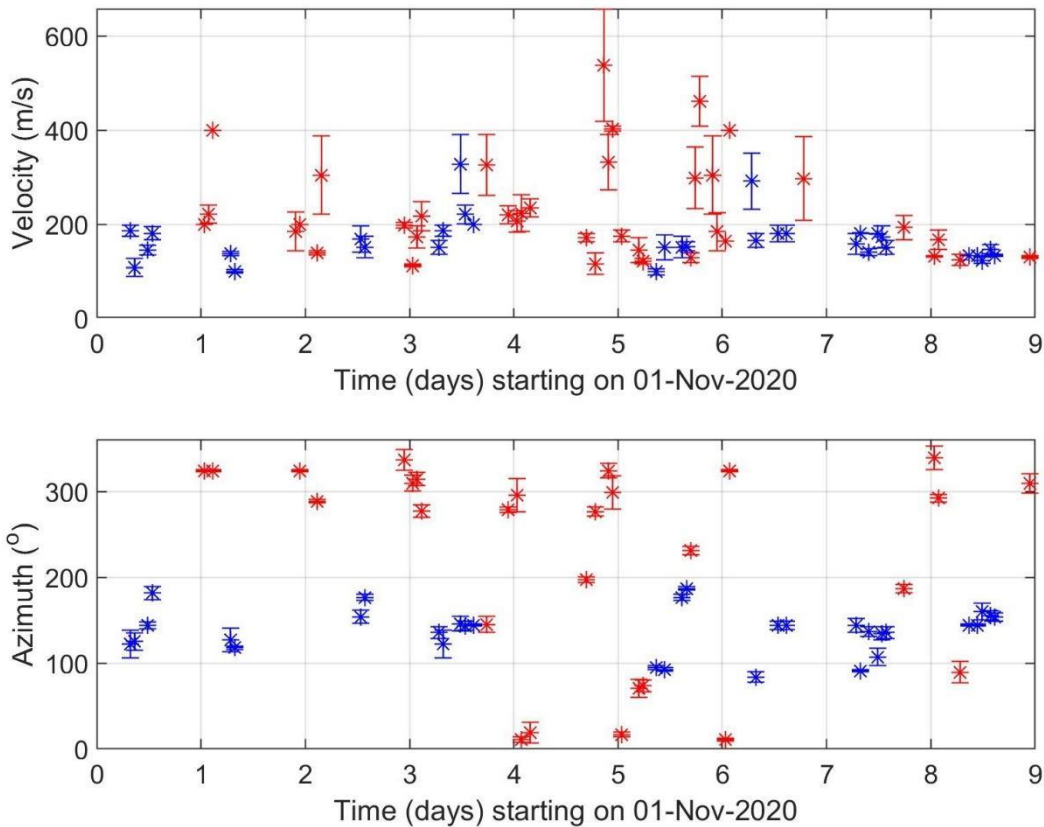
581 **Figure 13** GW characteristics (RMS of pressure fluctuations, phase velocity and azimuth)  
 582 for calm periods (upper plots) and streamer and streamer like events (bottom plots) for 2020  
 583 and winter 2021. The red vertical lines mark lower (Q1) and upper (Q3) quartiles. The dashed  
 584 magenta vertical lines depict boundaries for large ( $Q3+1.5 \cdot (Q3-Q1)$ ) and extreme ( $Q3+3 \cdot (Q3-$   
 585  $Q1)$ ) values.

586

### 587 3.2.2 Investigation of GWs measured in the ionosphere by continuous Doppler 588 sounding system (CDS)

589 The 2D propagation analysis of GWs was performed using the 2D versions of methods  
 590 mentioned in Section 2 and in detail described by Chum and Podolská (2018). As discussed in  
 591 Section 2 and by (Chum et al., 2021), the 2D propagation analysis makes it possible to  
 592 analyze much larger number of time intervals than the 3D analysis. The propagation analysis  
 593 obtained for the interval from 1<sup>st</sup> November to 9<sup>th</sup> November 2020, which covers the  
 594 significant streamer event that occurred from 3<sup>rd</sup> November 2020 to 7<sup>th</sup> November 2020, is  
 595 presented in Figure 14. Only results that satisfied the criteria ( $dv/v < 0.2$ ) and ( $dAZ < 20^\circ$ ) and

596 ( $f_{\text{DRMS}} > 0.05$  Hz) and ( $C_{\text{max}} < 0.5$ ) are presented, where  $dv/v$  is the relative uncertainty of GW  
597 phase velocity,  $dAZ$  is the azimuth uncertainty,  $f_{\text{DRMS}}$  is the root mean square of the Doppler  
598 shift in the analysed time interval and  $C_{\text{max}}$  is the maximum in the normalized energy map for  
599 the best beam (slowness) search;  $C_{\text{max}}$  is 1 for identical signals (Chum and Podolská, 2018). It  
600 is considered that signals are not sufficiently correlated (coherent) for reliable propagation  
601 analysis if  $C_{\text{max}} < 0.5$  (Chum et al., 2021). The velocities and azimuth obtained by observation  
602 at 3.59 MHz are in red, whereas the values based on measurements at 4.65 MHz are in blue.  
603 Obviously, the observations at 3.59 MHz mostly correspond to the nighttime, whereas  
604 observations at 4.65 MHz were mostly made during the daytime. The 4.65 MHz signal did not  
605 reflect from the ionosphere (escaped to the outer space) at night due to the low critical  
606 frequency of the ionosphere. On the other hand, the 3.59 MHz signal mostly reflected during  
607 the day from the ionospheric E layer and the Doppler shift was negligible, difficult to  
608 analyse. The GWs usually propagated roughly poleward at night and roughly equatorward  
609 during the daytime. This is fully consistent with the statistical investigation (Chum et al.,  
610 2021) which showed that propagation directions of GWs in the ionosphere exhibit diurnal and  
611 seasonal behaviour and are mainly controlled by the neutral winds in the thermosphere.



612

613 **Figure 14** Propagation velocity and azimuth of GWs in the ionosphere obtained using CDS  
614 measurements from 2020-11-01 to 2020-11-09. The velocities and azimuth obtained by  
615 observation at 3.59 MHz are by red, whereas the values based on measurements at 4.65 MHz  
616 are by blue.

617 Based on the analysis of the GW observed in the ionosphere during the streamer event and  
618 on the previous statistical analysis, we conclude that no obvious signature related to streamer  
619 event was observed for the propagation of GW the ionosphere.

620 It should be also mentioned that the phase velocities of GW measured on the ground (Figure  
621 8) and at heights around 200 km in the ionosphere differ. There are several reasons for that.  
622 First, the observed horizontal phase velocities depend on the elevation angle of GW  
623 propagation and on the ambient temperature as follows from the dispersion relation (the  
624 temperature enters the dispersion relation via the buoyancy frequency and the scale height).  
625 The temperature in the ionosphere/thermosphere is several times higher than in the  
626 troposphere. The elevation angles might change during the upward propagation of GWs,  
627 depending on the wind and temperature profile. Second, GWs propagate with a tilt, not  
628 vertically upward. It is therefore highly probable that the sources of the GWs observed in the  
629 troposphere and ionosphere are different. Moreover, GW can break during their propagation  
630 upward and secondary gravity waves might be observed in the ionosphere.

#### 631 **4) Conclusion and discussion**

632 The focus of this study was to test independent types of observations like Doppler sounding  
633 and microbarograph measurements for an analysis of GW behavior during streamer events,  
634 which are strongly connected with PW or GW and the large scale mass transport of ozone and  
635 that is why it can be very interesting for studies of atmospheric dynamics.

636 We also investigated infrasound propagation during streamer events, since modifications of  
637 infrasound ducting in the atmosphere can be expected in these periods. We evaluated  
638 infrasound detections at two microbarograph arrays in Central Europe during streamer events  
639 and compared them with observation during adjacent quiet periods. To obtain an overview of  
640 infrasound propagation from the source region to the region of observations, InfraGA/GeoAc  
641 raytracing tools (Blom and Waxler, 2012; Blom, 2019) were employed. In general, geometric  
642 acoustic approximation (raytracing) and the full wave models are used for simulations of  
643 infrasound propagation through the atmosphere. The great advantage of the full wave models  
644 is that they capture the leaking of energy between the waveguides. Waxler and Assink (2019)

645 emphasize particularly energy leaking between the tropospheric and stratospheric waveguide.  
646 Geometrical acoustics approximation provides an easy-to-interpret model of infrasound  
647 propagation in the atmosphere at lower computational costs compared to the full wave  
648 models. Its disadvantage is that the geometrical acoustics approximation assumes no energy  
649 propagation in the forbidden regions (for details see e.g. Waxler and Assink, 2019) and thus  
650 provides a model of infrasound propagation in separated waveguides. Available methods of  
651 infrasound propagation simulations are in detail discussed by Waxler and Assink (2019). The  
652 approximation of atmospheric wave ducts provided by the raytracing was sufficient for the  
653 purpose of our study; we aimed to obtain an elemental picture of infrasound propagation  
654 during the periods of interest; it means to identify which wave guides are formed, their  
655 directivity, and spatial extent.

656 The InfraGA/GeoAc predicts that a waveguide develops at the tropopause during the  
657 analyzed streamer events in November 2020 and in March 2021 the direction of which is  
658 determined by the disturbed jet-stream. The tropopause waveguide ducts infrasound up to  
659 distances of several hundreds to a thousand of km from the source in a limited azimuth range.  
660 The azimuth sector of the extent of  $50 - 60^\circ$  is influenced in the analysed cases.

661 In accord with the model predictions, phenomena that can be unambiguously attributed to  
662 streamer event effects were not found in infrasound detections at the infrasound stations PSCI  
663 and WBCI during the studied cases. We assume that the observability of streamer event  
664 signatures in infrasound arrival parameters depends on the mutual position of the source, the  
665 streamer event disturbance of the tropopause jet-stream and the infrasound station. It can be  
666 recommended for future studies to use a dense network of infrasound arrays that covers  
667 various directions and distances from the streamer event. Due to the typical occurrence of the  
668 streamer events over the North Atlantic, infrasound stations in Western Europe are of  
669 particular interest.

670 Supplementary ground-based measurements of GW using the WBCI array in the troposphere  
671 showed that GW propagation azimuths were more random during streamer and streamer-like  
672 events compared to those observed during calm conditions as can be seen from the plots in  
673 Figure 13. On the other hand, the GW propagation characteristics observed in the ionosphere  
674 by CDS during streamer events did not differ from those expected for the given time period,  
675 based on previous statistical studies (Chum et al., 2021).

676 The results therefore indicate that streamers in the stratosphere might lead to changes in wave  
677 propagation in the troposphere. The impact on the ionosphere was not confirmed, but cannot

678 be excluded due to sparse and localized observations of GW activity. In general, to validate the  
679 preliminary results obtained in this study, a denser measurement network and more streamer  
680 events need to be analyzed.

681

#### 682 **Data availability:**

683 ozone column measurements (TCO) which are available as a service by DLR at

684 <https://atmos.eoc.dlr.de/>

685 Ground to space model vertical atmospheric profiles were obtained at

686 <https://g2s.ncpa.olemiss.edu/>; accessed on 27 January – 4 February 2024

687

688 The WAVEWATCHIII<sup>®</sup> wave-action model data were accessed via ftp at

689 [polar.ncep.noaa.gov/waves/JCOMM/2020](ftp://polar.ncep.noaa.gov/waves/JCOMM/2020) on 13-14 March 2023.

690

691 The Deutscher Wetterdienst synoptic charts were accessed at

692 [https://www2.wetter3.de/archiv\\_dwd\\_dt.html](https://www2.wetter3.de/archiv_dwd_dt.html) on 3 February 2024.

693

#### 694 **Author contributions**

695 MK and LK create the idea of manuscript; JCh, MK, TS, LK, and KP suggest the datasets and  
696 methods; TS, JCh, LK, KP and FT analyzed the data; MK wrote the manuscript draft; JCh,  
697 TS, LK and KP reviewed and edited the manuscript.

#### 698 **Competing interests**

699 The authors declare that they have no conflict of interest.

700

#### 701 **Acknowledgement**

702 The DTK-GPMCC software was kindly provided by Commissariat à l'énergie atomique et  
703 aux énergies alternatives, Centre DAM-Île-de-France, Département Analyse, Surveillance,  
704 Environnement, Bruyères-le-Châtel, F91297 Arpajon, France.

705 The authors are grateful to Dr. Phil Blom and Los Alamos National Laboratory for opening  
706 the InfraGA/GeoAc tools to the public.

707 We also acknowledge [earth.nullschool.net](http://earth.nullschool.net) for providing the figures.



708 **Financial support:** This study is supported by LISA project- Lidar measurements to  
709 Identify Streamers and analyze Atmospheric waves, AEOLUS-INNOVATION, Contract No.  
710 4000133567/20/I-BG

711

## 712 **References**

713 Assink, J.D., Waxler, R., Smets, P., Evers, L.G. (2014). Bidirectional infrasonic ducts  
714 associated with sudden stratospheric warm-ing events. *J. Geophys. Res. Atmos.* 119,1140-  
715 1153.

716 Bittner, M., Höppner, K., Pilger, C., Schmidt, C. (2010). Mesopause temperature  
717 perturbations caused by infrasonic waves as a potential indicator for the detection of  
718 tsunamis and other geo-hazards. *Nat. Hazards Earth Syst. Sci.*, 10, 1431-1442. [www.nat-](http://www.nat-hazards-earth-syst-sci.net/10/1431/2010/doi:10.5194/nhess-10-1431-2010)  
719 [hazards-earth-syst-sci.net/10/1431/2010/doi:10.5194/nhess-10-1431-2010](http://www.nat-hazards-earth-syst-sci.net/10/1431/2010/doi:10.5194/nhess-10-1431-2010)

720 Blanc, E. (1985). Observations in the upper atmosphere of infrasonic waves from natural or  
721 artificial sources: A summary. *Ann. Geophys.*, 3, 673-688.

722 Blixt, E.M., Nasholm, S.P., Gibbons, S.J., Evers, L.G., Charlton-Perez, A.J., Orsolini, Y.J.,  
723 Kvaerna, T. (2019). Estimating tropo-spheric and stratospheric winds using infrasound from  
724 explosions. *J. Acoust. Soc. Am.* 146:2.

725 Blom, P., Waxler, R. (2012). “Impulse propagation in the nocturnal boundary layer: Analysis  
726 of the geometric component”. *J. Acoust. Soc. Am.*, **131**, 3680 – 3690. doi:  
727 [10.1121/1.3699174](https://doi.org/10.1121/1.3699174).

728 Blom, P. (2019). “Modeling infrasonic propagation through a spherical atmospheric layer:  
729 Analysis of the stratospheric pair.” *J. Acoust. Soc. Am.*, **145**, 2198–2208. doi:  
730 [10.1121/1.5096855](https://doi.org/10.1121/1.5096855).

731 Bondár I., T. Šindelářová, D. Ghica, U. Mitterbauer, A. Liashchuk, J. Baše, J. Chum, C.  
732 Czanik, C. Ionescu, C. Neagoe, M. Pásztor, A. Le Pichon (2022), Central and Eastern  
733 European Infrasound Network: Contribution to Infrasound Monitoring, *Geophys. J. Int.*,  
734 ggac066, <https://doi.org/10.1093/gji/ggac066>

735 Brachet, N., Brown, D., Le Bras R., Cansi, Y., Mialle, P., Coyne, J. (2010). Monitoring the  
736 Earth's Atmosphere with the Global IMS Infrasound Network. In: Le Pichon, A., Blanc, E.,  
737 Hauchecorne A. (Eds.), *Infrasound Monitoring for Atmospheric Studies*. Springer  
738 Science+Business Media B.V., 77-118. Doi: 10.1007/978-1-4020-9508-5\_3

739 Campus, P., Christie, D.R. (2010). Worldwide Observations of Infrasonic Waves. In: Le  
740 Pichon, A., Blanc, E., Hauchecorne A. (Eds.), *Infrasound Monitoring for Atmospheric  
741 Studies*. Springer Science+Business Media B.V., 185234-118. Doi: 10.1007/978-1-4020-  
742 9508-5\_6

743 Cansi, Y., 1995. An automatic seismic event processing for detection and location: The  
744 P.M.C.C. method. *Geophys. Res. Lett.* 22, 1021-1024. doi: 10.1029/95GL00468

745 Ceranna, L., Matoza, R., Hupe, P., Le Pichon, A., Landès, M., (2019). Systematic Array  
746 Processing of a Decade of Global IMS Infrasound Data. In: Le Pichon, A., Blanc, E.,  
747 Hauchecorne, A. (eds) *Infrasound Monitoring for Atmospheric Studies. Chal-lenges in  
748 Middle Atmospheric Dynamics and Societal Benefits*. Springer Nature Switzerland AG.

749 Chum J, Podolská K (2018) 3D analysis of GW propagation in the ionosphere. *Geophysical  
750 Research Letters*, 45, 11,562–11,571, <https://doi.org/10.1029/2018GL07969>

751 Chum, J., Podolská, K., Ruzs, J., Baše, J., Tedoradze, N. (2021), Statistical investigation of  
752 gravity wave characteristics in the ionosphere. *Earth Planets Space* 73, 60,  
753 <https://doi.org/10.1186/s40623-021-01379-3>

754 Czech microbarograph network, <https://doi.org/10.7914/SN/C9>

755 Drob, D. P., Picone, J. M., Garcés, M. (2003). Global morphology of infrasound propagation.  
756 *J. Geophys. Res. Atmospheres*, **108** (D21). doi: [10.1029/2002JD003307](https://doi.org/10.1029/2002JD003307).

757 Evers, L. G., Siegmund, P. (2009). Infrasonic signature of the 2009 major sudden  
758 stratosphericwarming, *Geophys. Res. Lett.*, 36, L23808, doi:10.1029/2009GL041323

759 Evers, L.G., Haak, H.W. (2010). The Characteristics of Infrasound, its Propagation and Some  
760 Early History. In: Le Pichon, A., Blanc, E., Hauchecorne, A. (eds) *Infrasound Monitoring for  
761 Atmospheric Studies*. Springer, Dordrecht.

762 Evers, L. G., van Geyt, A. R. J. , Smets, P., Fricke, J.T. (2012). Anomalous infrasound  
763 propagation in a hot stratosphere and the existence of extremely small shadow zones, *J.*  
764 *Geophys. Res.*, 117, D06120, doi:10.1029/2011JD017014.

765

766 Eyring, V., Dameris, M., Grewe, V., Langbein, I., & Kouker, W. (2002). Climatologies of  
767 streamer events derived from a transport model and a coupled chemistry-climate model.

768 Fritts, D.C. & Alexander, M.J., (2003). Gravity wave dynamics and effects in the middle  
769 atmosphere. *Rev. Geophys.*, 41 (1), 1003.

770 Garcès, M., Willis, M., Hetzer, C., Le Pichon , A., Drob, D., (2004). On using ocean swells  
771 for continuous infrasonic measurements of winds and temperature in the lower, middle, and  
772 upper atmosphere. *Geophys. Res. Lett.* 31, L19304. doi: 10.1029/2004GL020696

773 Garcès, M.A., (2013). On infrasound standards, part 1: Time, frequency, and energy scaling.  
774 *InfraMatics* 2, 13-35. doi: 10.4236/inframatics.2013.22002

775 Georges, T.M. (1968). H. F. Doppler studies of travelling ionospheric disturbances. *J.*  
776 *Atmos.Terr. Phys.*, 30, 735-746.

777 Gerlach, C., Földvary, L., Švehla, D., Gruber, T., Wermuth, M., Sneeuw, N., ... &  
778 Steigenberger, P. (2003). A CHAMP-only gravity field model from kinematic orbits using the  
779 energy integral. *Geophysical Research Letters*, 30(20).

780 Hersbach, H., Bell, B., Berrisford, P., Hirahara, S., Horányi, A., Muñoz-Sabater, J., ... &  
781 Thépaut, J. N. (2020). The ERA5 global reanalysis. *Quarterly Journal of the Royal*  
782 *Meteorological Society*, 146(730), 1999-2049.

783 Hupe, P., Ceranna, L., Pilger, C., de Carlo, M., Le Pichon, A., Kaifler, B., Rapp, M. (2019).  
784 Assessing middle atmosphere weather models using infrasound detections from microbaroms.  
785 *Geophys. J. Int.*, 216, 1761–1767 doi: 10.1093/gji/ggy520

786 James, P. M. (1998): A climatology of ozone mini-holes over the Northern Hemisphere.  
787 *International Journal of Climatology: A Journal of the Royal Meteorological Society*, 18, 12:  
788 12871303

789 Kramer, R, S. Wüst, and M. Bittner (2016). Investigation of gravity wave activity based on  
790 operational radiosonde data from 13 years (1997-2009): Climatology and possible induced  
791 variability, *Journal of Atmospheric and Solar-Terrestrial Physics* 140, 23–33;  
792 <http://dx.doi.org/10.1016/j.jastp.2016.01.014>

793 Kramer, R., S. Wüst, C. Schmidt, and M. Bittner (2015). Gravity wave characteristics in the  
794 middle atmosphere during the CESAR campaign at Palma de Mallorca in 2011/2012: Impact  
795 of extratropical cyclones and cold fronts, *Journal of Atmospheric and Solar-Terrestrial*  
796 *Physics* 128 (2015) 8–23, <http://dx.doi.org/10.1016/j.jastp.2015.03.001>

797 Kai Ming Huang, Shao Dong Zhang, Fan Yi, (2010). Reflection and transmission of  
798 atmospheric gravity waves in a stably sheared horizontal wind field, *Journal of Geophysical*  
799 *Research: Atmospheres*, 10.1029/2009JD012687, **115**, D16,

800 Landès, M., Ceranna, L., Le Pichon, A., & Matoza, R. S. (2012). Localization of microbarom  
801 sources using the IMS infrasound network. *Journal of Geophysical Research:*  
802 *Atmospheres*, 117(D6).

803 Le Pichon, A., Cansi, Y. (2003). PMCC for infrasound data processing. *InfraMatics* 02, 1-9.

804 Le Pichon, A., Blanc, E., (2005). Probing high-altitude winds using infrasound. *J. Geophys.*  
805 *Res.*, 110, D20104. doi: 10.1029/2005JD006020

806 Le Pichon, A., Ceranna, L., Garcès, M., Drob, D., Millet, C., (2006). On using infrasound  
807 from interacting ocean swells for global continuous measurements of winds and temperature  
808 in the stratosphere. *J. Geophys. Res.*, 111, D11106. doi: 10.1029/2005JD006690

809 Le Pichon, A., Vergoz, J., Blanc, E., Guilbert, J., Ceranna, L., Evers, L., Brachet, N., (2009).  
810 Assessing the performance of the International Monitoring System's infrasound network:  
811 Geographical coverage and temporal variabilities. *J. Geophys. Res.* 114, D08112. doi:  
812 10.1029/2008JD010907

813 Leovy, C. B., Sun, C. R., Hitchman, M. H., Remsberg, E. E., Russell III, J. M., Gordley, L.  
814 L., ... & Lyjak, L. V. (1985). Transport of ozone in the middle stratosphere: Evidence for  
815 planetary wave breaking. *Journal of Atmospheric Sciences*, 42(3), 230-244.

816 Lonzaga, J.B., (2015). A theoretical relation between the celerity and trace velocity of  
817 infrasonic phases, *J. Acoust. Soc. Am.*, 138, EL242-EL247.  
818 <http://dx.doi.org/10.1121/1.4929628>

819 Loyola D.G., Koukouli M.E., Valks P., Balis D.S., Hao N., van Roozendaal M., Spurr R.J.D.,  
820 Zimmer W., Kiemle S., Lerot C., Lambert J.-C. (2011) The GOME-2 total column ozone  
821 product: Retrieval algorithm and ground-based validation, *Journal of Geophysical Research*,  
822 vol. 116, D07302, Wiley-Blackwell

823 Marty, J., (2019). The IMS Infrasound Network: Current Status and Technological  
824 Developments, in: Le Pichon, A., Blanc, E., Hauchecorn, A. (Eds.), *Infrasound Monitoring*  
825 *for Atmospheric Studies. Challenges in Middle Atmosphere Dynamics and Societal Benefits*.  
826 Springer Nature Switzerland AG, pp. 3–62. doi:10.1007/978-3-319-75140-5\_1

827 McIntyre, M. E., & Palmer, T. N. (1983). Breaking planetary waves in the stratosphere.  
828 *Nature*, 305(5935), 593-600.

829 Munro, R., Eisinger, M., Anderson, C., Callies, J., Corpaccioli, E., Lang, R., ... & Albinana,  
830 A. P. (2006, June). GOME-2 on MetOp. In *Proc. of The 2006 EUMETSAT Meteorological*  
831 *Satellite Conference*, Helsinki, Finland (Vol. 1216, p. 48).

832 Munro, R., et al. (2016): The GOME-2 instrument on the Metop series of satellites:  
833 instrument design, calibration, and level 1 data processing – an overview, *Atmos. Meas.*  
834 *Tech.*, 9, 1279–1301, <https://doi.org/10.5194/amt-9-1279-2016>.

835 Peters, D., Hoffmann, P., & Alpers, M. (2003). On the appearance of inertia-gravity waves on  
836 the north-easterly side of an anticyclone. *Meteorologische Zeitschrift*, 12(1), 25-35

837 Polvani, L. M., & Plumb, R. A. (1992). Rossby wave breaking, microbreaking, filamentation,  
838 and secondary vortex formation: The dynamics of a perturbed vortex. *Journal of Atmospheric*  
839 *Sciences*, 49(6), 462-476.

840 Pramitha, M., Venkat Ratnam, M., Taori, A., Krishna Murthy, B. V., Pallamraju, D., and  
841 Vijaya Bhaskar Rao, S. (2015). Evidence for tropospheric wind shear excitation of high-  
842 phase-speed gravity waves reaching the mesosphere using the ray-tracing technique, *Atmos.*  
843 *Chem. Phys.*, 15, 2709–2721, <https://doi.org/10.5194/acp-15-2709-2015>.

844 Rauthe, M., Gerding, M., Höffner, J., & Lübken, F. J. (2006). Lidar temperature  
845 measurements of gravity waves over Kühlungsborn (54° N) from 1 to 105 km: A winter-  
846 summer comparison. *Journal of Geophysical Research: Atmospheres*, 111(D24).  
847

848 Wüst, S., & Bittner, M. (2006). Non-linear resonant wave–wave interaction (triad): Case  
849 studies based on rocket data and first application to satellite data. *Journal of atmospheric and*  
850 *solar-terrestrial physics*, 68(9), 959-976.  
851

852 Wüst, S., Offenwanger, T., Schmidt, C., Bittner, M., Jacobi, C., Stober, G., Yee, J.H.,  
853 Mlynczak, M. G. & Russell III, J. M. (2018). Derivation of gravity wave intrinsic parameters  
854 and vertical wavelength using a single scanning OH (3-1) airglow spectrometer. *Atmospheric*  
855 *Measurement Techniques*, 11(5), 2937-2947.  
856

857 Smets, P.S.M., Evers, L.G. (2014). The life cycle of a sudden stratospheric warming from  
858 infrasonic ambient noise observations, *J. Geophys. Res. Atmos.*, 119, 12,084-12,099

859 Spurr, R., Loyola, D., Heue, K. P., Van Roozendael, M., & Lerot, C. (2022). S5P/TROPOMI  
860 Total Ozone ATBD. Deutsches Zentrum für Luft- und Raumfahrt (German Aerospace  
861 Center), Weßling, Germany, Tech. Rep. S5P-L2-DLR-ATBD-400A.

862 Sutherland, L.C., Bass, H.E., (2004). Atmospheric absorption in the atmosphere up to 160  
863 km. *J. Acoust. Soc. Am.*, 115, 1012–1032. <https://doi.org/10.1121/1.1631937>

864 Szuberla, C.A.L., Olson, J.V., (2004). Uncertainties associated with parameter estimation in  
865 atmospheric infrasound rays. *J. Acoust. Soc. Am.* 115, 253-258. doi: 10.1121/1.1635407

866 Veefkind, J. P., Aben, I., McMullan, K., Förster, H., De Vries, J., Otter, G., ... & Levelt, P. F.  
867 (2012). TROPOMI on the ESA Sentinel-5 Precursor: A GMES mission for global  
868 observations of the atmospheric composition for climate, air quality and ozone layer  
869 applications. *Remote sensing of environment*, 120, 70-83.

870 Waxler, R., Assink, J., 2019. Propagation Modeling Through Realistic Atmosphere and  
871 Benchmarking, in: Le Pichon, A., Blanc, E., Hauchecorn, A. (Eds.), *Infrasound Monitoring*  
872 *for Atmospheric Studies. Challenges in Middle Atmosphere Dynamics and Societal Benefits.*  
873 Springer Nature Switzerland AG, pp. 3–62. doi:10.1007/978-3-319-75140-5\_15  
874  
875